

## Rising from the Ashes II: Can Bar Formation Lead to Abundance Bimodalities?

ANGUS BEANE,<sup>1</sup> JAMES W. JOHNSON,<sup>2</sup> VADIM SEMENOV,<sup>1</sup> LARS HERNQUIST,<sup>1</sup> VEDANT CHANDRA,<sup>1</sup> AND CHARLIE CONROY<sup>1</sup>

<sup>1</sup>*Center for Astrophysics | Harvard & Smithsonian, Cambridge, MA, USA*

<sup>2</sup>*Carnegie Science Observatories, Pasadena, CA, USA*

### ABSTRACT

The Milky Way is known to host at least two modes in its present day distribution of Fe and  $\alpha$ -elements. The exact cause of this bimodality is disputed, but one class of explanations involves the merger between the Milky Way and a relatively massive satellite (Gaia-Sausage-Enceladus) at  $z \sim 2$ . However, reproducing this bimodality in simulations is not straightforward, with conflicting results on the prevalence, morphology, and mechanism behind multimodality. We present a case study of a galaxy in the Illustris TNG50 simulation which undergoes a sequence of starburst, brief quiescence, and then rejuvenation. Following a minor post-processing adjustment — motivated by recent findings on the star formation efficiency in TNG — which increases the  $[\alpha/\text{Fe}]$  values of older star particles, we demonstrate that this galaxy exhibits a pronounced bimodal distribution in the  $[\alpha/\text{Fe}]-[\text{Fe}/\text{H}]$  plane. The high- and low- $\alpha$  sequences are neatly separated in time by the brief quiescent period. The quiescent period in this galaxy is not associated with a merger but by the formation of a bar followed by AGN activity. This galaxy indicates a novel scenario in which the  $\alpha$ -bimodality is caused by AGN-induced quenching triggered by the formation of the Milky Way’s bar. We argue that the post-processing step can be interpreted as the TNG model underproducing star formation in the densest regions at high- $z$ .

**Keywords:** Classical Novae (251) — Ultraviolet astronomy(1736) — History of astronomy(1868) — Interdisciplinary astronomy(804)

### 1. INTRODUCTION

The stellar surface abundances of most elements retain the composition of their natal gas cloud. Therefore, the present-day distribution of their abundances encodes the chemical history of a galaxy’s gas phase. Two classes elements have received particular attention in the Milky Way due to their disparate formation channels: iron-peak (such as Fe) and  $\alpha$ -elements (produced through the  $\alpha$ -process, such as O and Mg). Iron-peak elements are produced in both Type Ia and Type II supernovae (SNe) whereas  $\alpha$ -elements are produced predominantly through Type II SNe. In the Milky Way, there is a well-established bimodality with separate high- and low- $\alpha$  sequences shown in Figure 1 (Gratton et al. 1996; Fuhrmann 1998, 2004; Reddy et al. 2006; Adibekyan et al. 2011, 2012; Bensby et al. 2014; Nidever et al. 2014; Hayden et al. 2020).

Broadly speaking, there are three approaches to explaining the bimodality. First, it is a result of internal secular processes that generate the bimodality through radial migration (Schönrich & Binney 2009; Sharma et al. 2021; Chen et al. 2023) or clump formation (Clarke et al. 2019; Beraldo e Silva et al. 2020, 2021; Garver et al. 2023). Second, the bimodality is generated through gas infall scenarios, either from specific gas accretion episodes from the intergalactic medium

(Chiappini et al. 1997; Chiappini 2009; Grisoni et al. 2017; Spitoni et al. 2019), or through a more self-consistent collapse sequence of the circumgalactic medium driven through feedback (Khoperskov et al. 2021). Third and finally, the bimodality is generated through a merger process, either by enhancing the star formation rate (SFR) of the Galaxy (Brook et al. 2004, 2005, 2007; Richard et al. 2010) or by supplying a relatively pristine gas supply that resets the metallicity of the Galaxy (Buck 2020; Ciucă et al. 2024). Strong evidence that the Milky Way did undergo a merger with the Gaia-Sausage-Enceladus (GSE) satellite supports these scenarios (Belokurov et al. 2018; Helmi et al. 2018; Naidu et al. 2020; Chandra et al. 2024).

In Beane (2024) (hereafter Paper I), we proposed an alternate scenario for the formation of the bimodality, driven by a brief ( $\sim 300$  Myr) quiescent period in the Galaxy’s history, which has two effects. First, the reduced SFR lowers the number of  $\alpha$ -producing Type II SNe relative to Type Ia<sup>1</sup>, causing a sharp decline in the  $[\alpha/\text{Fe}]$  ratio in the star-forming

<sup>1</sup> These SNe occur on different timescales (10s of Myr after star formation for Type II, as compared to 100s of Myr to Gyrs for Type Ia), so if the SFR drops, the number of Type II SNe drops faster than Type Ia.

gas. Second, the lower SFR results in fewer stars forming in the region between the high- and low- $\alpha$  sequences, reducing the occurrence of this transitional population in present-day observations. This mechanism resembles two-phase infall models that incorporate a temporary halt in star formation (Spitoni et al. 2024, and references therein), though the quiescent period in Paper I is much shorter. The combination of these two effects creates the valley between the high- and low- $\alpha$  sequences.

In Paper I, we used idealized simulations of a galaxy merger that triggered the quiescent period. However, we argued that the merger aspect of that work was not necessary. In this work, we study a subhalo, or galaxy, from the Illustris TNG50 simulation demonstrating this. This subhalo of interest (SoI) exhibits the sequence of events presented in Paper I after a simple post-processing step which increases the  $[\alpha/\text{Fe}]$  of old star particles. This post-processing is motivated by recent work demonstrating that the star formation efficiency (SFE) of the dense gas present at high- $z$  is too low (Hassan et al. 2024). The SoI undergoes a brief quiescent period which neatly separates a high- and low- $\alpha$  sequence. However, instead of being preceded by a merger, the quenching is preceded by apparent bar-induced AGN activity. Therefore, this work serves as a verification that the scenario in Paper I is possible in cosmological simulations and does not require a merger.

In Section 2 we discuss our selection technique which led to discovering the SoI, the observations we use for comparison, as well as a simple one zone chemical evolution model we use to justify our post-processing step. In Section 3 we present the main results which we discuss and interpret in Section 4. We conclude in Section 5.

## 2. METHODS

### 2.1. IllustrisTNG Sample

We use Illustris TNG50 (Pillepich et al. 2019; Nelson et al. 2019), a cosmological simulation of a  $\sim 50$  cMpc box at high resolution ( $m_{\text{baryon}} \sim 8.5 \times 10^4 M_{\odot}$ ). It uses the gravito-magneto-hydrodynamics code AREPO (Springel 2010; Pakmor et al. 2016), along with the TNG model (Vogelsberger et al. 2013; Weinberger et al. 2017; Pillepich et al. 2018). This model includes several subgrid processes: a wind generation model, chemical enrichment from SNe and asymptotic giant branch stars, and thermal and kinetic feedback from AGN.

One piece of the TNG model of note for this work is the black hole (BH) accretion and feedback method (Weinberger et al. 2017). The BH accretion rate ( $\dot{M}_{\text{BH}}$ ) is computed using the local structure of the gas phase with the Bondi-Hoyle-Lyttleton formula (Hoyle & Lyttleton 1939; Bondi & Hoyle 1944; Bondi 1952), with a maximum of the Eddington accretion rate ( $\dot{M}_{\text{edd}}$ ). The model allows the BH to be either in a kinetic radio-mode or a thermal quasar-mode. If the Eddington ratio ( $\dot{M}_{\text{BH}}/\dot{M}_{\text{edd}}$ ) exceeds a threshold ( $M_{\text{BH}}$ -dependent,

dark matter	
$M_{200}$	$4.97 \times 10^{12} M_{\odot}$
$R_{200}$	532 kpc
baryons	
$r_{\star, \text{half}}$	2 kpc
$M_{\text{star}}(r < 4r_{\star, \text{half}})$	$7.6 \times 10^{12} M_{\odot}$
$M_{\text{gas}}(r < 4r_{\star, \text{half}})$	$2.6 \times 10^{11} M_{\odot}$
SFR	$0.56 M_{\odot}/\text{yr}$
$M_{\text{BH}}$	$2.9 \times 10^8 M_{\odot}$
$\dot{M}_{\text{BH}}/\dot{M}_{\text{edd}}$	$4.5 \times 10^{-5}$

**Table 1.** Summary statistics of our subhalo of interest at  $z = 0$ .  $M_{200}$  and  $R_{200}$  are relative to the mean density of the universe, the SFR is for all gas bound to the subhalo, and the BH refers to the central BH.

but  $\sim 0.001$ – $0.1$ ), the BH is in the quasar mode and injects a large amount of thermal energy into its surroundings.

Using the public catalog, we selected a sample of subhalos at  $z = 1.5$  (snapshot 40) according to the following criteria: (1) the subhalo is central (i.e., the most massive subhalo within its halo), and (2) the subhalo’s stellar mass is between  $10^{10}$  and  $10^{10.5} M_{\odot}/h$ . There were a total of 168 subhalos that met both criteria. The chosen mass range is broadly consistent with the expected mass of the Milky Way at this redshift (van Dokkum et al. 2013). We choose to make our selection of galaxies at  $z = 1.5$  instead of at lower redshift because we wish to capture the *formation* of multimodal structure. Mergers at lower redshift contribute very little to the Milky Way’s disk stars (e.g., Bland-Hawthorn & Gerhard 2016), and would act as a contaminant in our sample.

We examine the abundance distribution in the  $[\text{Mg}/\text{Fe}]$ – $[\text{Fe}/\text{H}]$  plane for this sample of subhalos by visual inspection. Few subhalos display multimodal structure, and when present, it is much weaker compared to that observed in the Milky Way. We then apply a post-processing step to the  $[\text{Mg}/\text{Fe}]$  of the stars, adding a value of  $0.1 \times (t_{1.5} - t_{\text{form}})$  to each star particle, where  $t_{1.5}$  is the age of the universe at  $z = 1.5$  ( $\sim 4.3$  Gyr), and  $t_{\text{form}}$  is the formation time of the star particle. After this adjustment, which we justify in Section 4.2 based on TNG underpredicting the SFE of dense gas, we observe that the abundance structure becomes significantly more pronounced.

We show the abundance distributions (replicating Figure 1) of 16 random subhalos from our catalog, and the subhalo we selected, in Appendix B. Of these subhalos, some structure is present, but none have a strong bimodality as seen in the Milky Way. After the  $\alpha$ -enhancement, a few have strongly bimodal features (subject to interpretation): 172175, 178140, 193025.

We select subhalo 172175 (the ID at snapshot 40) for its resemblance to the Milky Way. We then studied the main de-

scendant of this subhalo at  $z = 0$  (subhalo 392276 at snapshot 99). A summary of its key properties is given in Table 1. We refer to this subhalo as our subhalo of interest (SoI).

### 2.2. Observations

We make use of two observational data sets. First, we use the ASPCAP DR17 catalog of stellar abundances (García Pérez et al. 2016, J.A. Holtzman et al., in preparation). We make the same selection cuts as in Section 2.4 of Paper I. These criteria are meant to select giants with high quality abundance measurements as well as restricting the sample to only stars in the disk with angular momenta similar to the Sun’s. This results in a sample of 54,777 stars. We use Fe to track total metallicity and Mg alone as an  $\alpha$ -element.

We then further considered a dataset of stellar ages from the APOKASC2 catalog (Pinsonneault et al. 2018). This catalog uses a combination of APOGEE spectroscopic parameters and *Kepler* time series photometry to compute astroseismic ages. Using only stars with 25% age uncertainties (taken as the maximum of the upper and lower uncertainty), we cross-match this catalog to our larger sample from ASPCAP which results in a sample of 1201 stars.

### 2.3. One-Zone Chemical Evolution Model

James inserts his section

## 3. RESULTS

### 3.1. Abundance Plane

The main result of our paper is given in Figure 1. Here, we compare the abundance plane in the Milky Way (left column) to that of our subhalo of interest (middle and right columns). The upper panels show the 2D distribution in the space of  $[\text{Mg}/\text{Fe}]$ - $[\text{Fe}/\text{H}]$ . We have applied the standard *scipy* implementation of a gaussian kernel density estimator to a Cartesian grid of points. For each panel, we normalize so that the integral of the distribution is unity. Colors are plotted in a log scale ranging from 0.08 to 15  $\text{dex}^{-2}$ . Contour lines are plotted at 0.1, 1.5, and 10  $\text{dex}^{-2}$ .

The colored vertical regions are indicated at  $[\text{Fe}/\text{H}] = -0.75, -0.5, -0.25$ , and 0 dex in the Milky Way, and at bins 0.25 dex higher in the simulations. The lower panels show 1D histograms of  $[\text{Mg}/\text{Fe}]$  in bins centered on these values. The bins for the Milky Way/simulations have width 0.2/0.05 dex. The rationale for the higher plotted  $[\text{Fe}/\text{H}]$  in the simulations comes just from the empirical location of the bimodalities. The Milky Way shows a clear bimodal population, with a high- $\alpha$  sequence most clearly distinct from the low- $\alpha$  sequence at low metallicity. The two sequences merge around solar metallicity.

Our SoI, on the other hand, does not show a clearly bimodal structure in the fiducial simulation (middle column). There is some structure in the  $[\text{Fe}/\text{H}] = -0.75$  bin. The right panel of

Figure 1 shows the same distribution as in the middle panel, but with a post-processed declination in  $[\text{Mg}/\text{Fe}]$  described in Section 2.1. Star particles formed before  $z = 1.5$  are given an additive offset of  $0.1 \times (t_{1.5} - t_{\text{form}})$ , where  $t_{1.5}$  is the age of the universe at  $z = 1.5$  and  $t_{\text{form}}$  is the formation time of the star particle. A multimodal structure emerges with three clear modes at  $[\text{Mg}/\text{Fe}] \sim 0.8, 0.5$ , and 0.2 dex. The 1D histograms show that the modes are well-separated, and that the troughs between the modes nearly vanish.

### 3.2. Alpha Time Dependence

The abundance distributions shown in Figure 1 can be better understood by examining the evolution of  $[\text{Mg}/\text{Fe}]$  with time of the individual stars/star particles. In the upper panels of Figure 2 we show the true distribution of  $[\text{Mg}/\text{Fe}]$  as a function of time for the fiducial SoI in the middle and for the post-processed,  $\alpha$ -enhanced subhalo to the right. We use age instead of formation time in order to better facilitate comparisons to observations. These panels show 2D histograms, with a logarithmic colormap normalized to the maximum of the plot. To prevent overlap, the values of  $[\text{Mg}/\text{Fe}]$  are given offsets of 0, -0.5, -1, and -1.5, in order of increasing  $[\text{Fe}/\text{H}]$ .

In the SoI, there is an age gap at *sim*10.6 Gyr, which we mark with a vertical dashed line in the upper row. Star particles older than this line have a much clearer gradient in time with  $[\text{Mg}/\text{Fe}]$  than stars that form after. In the  $[\text{Fe}/\text{H}] = -0.25$  bin, star particles which form directly after this line have a slightly reduced  $[\text{Mg}/\text{Fe}]$  than stars which form a short time later.

In the lower row, the left panel shows data from the Milky Way, while the middle and right panels correspond to the fiducial and  $\alpha$ -enhanced SoI, respectively. For the simulations, we introduce Gaussian errors of 15% in age and 0.01 dex in  $[\text{Mg}/\text{Fe}]$ . These error values align with the observational uncertainties from the APOKASC2 and APOGEE datasets, which the Milky Way panel (lower left) is based on (see Appendix A for detailed plots of observational errors). While the error in  $[\text{Mg}/\text{Fe}]$  is relatively minor, the age error (1.5 Gyr at 10 Gyr) blurs the distribution, particularly around the dashed line that marks the transition between sequences. Despite this, the  $\alpha$ -enhanced SoI still shows two distinct populations, although their ages now overlap more significantly.

Interestingly, the Milky Way distribution (lower left panel) exhibits similarities to the  $\alpha$ -enhanced SoI. Specifically, in the  $[\text{Fe}/\text{H}] = -0.5$  and  $-0.25$  bins (blue and orange, respectively), there appear to be two populations that overlap in age but remain distinct in  $[\text{Mg}/\text{Fe}]$ . These are the bins where the bimodality is most pronounced (as seen in the upper left panel of Figure 1).

### 3.3. Evolutionary History

To understand the key events driving the behavior around the dashed line in Figure 2, we examine the evolution of

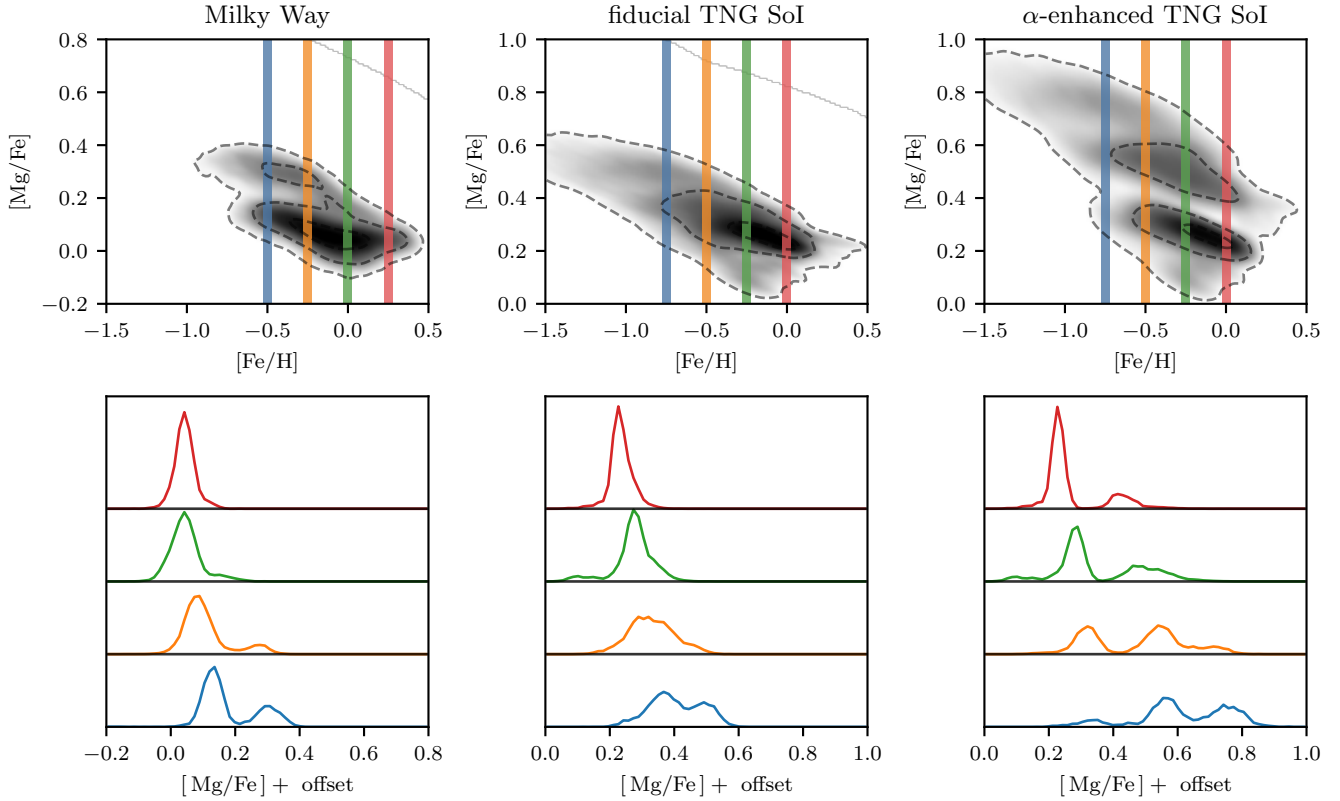


**Figure 1. When old stars are  $\alpha$ -enhanced, our subhalo of interest from TNG displays a prominent bimodality.** The upper left panel shows the distribution in the  $[\text{Mg}/\text{Fe}]$ - $[\text{Fe}/\text{H}]$  plane of the Milky Way, demonstrating a clear bimodality (data selection given in text). The lower left panel shows the 1D histograms of  $[\text{Mg}/\text{Fe}]$  at fixed  $[\text{Fe}/\text{H}]$  values of  $-0.5$ ,  $-0.25$ ,  $0$ , and  $0.25$  (blue, orange, green, and red, respectively). In the Milky Way, the bimodality is strongest at low metallicities while disappearing at high metallicities. The middle column shows the same plots but for our TNG subhalo of interest (392276) and with the fixed  $[\text{Fe}/\text{H}]$  values  $0.25$  dex lower. Only faint structure is seen in the lowest bin (blue,  $-0.75$  dex). The right column shows the same subhalo but after increasing the  $[\text{Mg}/\text{Fe}]$  value of star particles formed before  $z = 1.5$  linearly with formation time (with a slope of  $0.1\text{dex/Gyr}$ ). A clear bimodality is shown in these panels which, unlike in the Milky Way, is present at all metallicities.

several properties of the subhalo in Figure 3. The vertical dashed line in each panel marks the transition at  $t \sim 3.2$  Gyr from the high- to low- $\alpha$  sequences, as in Figure 2. The upper panel in the left column shows the SFR (computed for all gas cells in the subhalo). There are two peaks at  $t \sim 2.5$  Gyr and  $t \sim 4.5$  Gyr with maximum values of  $50 M_{\odot}/\text{yr}$  and  $30 M_{\odot}/\text{yr}$ , respectively. Around the high- to low- $\alpha$  transition, there is a dip in the SFR, which drops by an order of magnitude to about  $3 M_{\odot}/\text{yr}$ . The right panel zooms in on the period between  $t = 2$  Gyr and  $5$  Gyr, where we observe a sharp recovery in the SFR following the quiescent phase. In a single snapshot (spanning roughly  $150$  Myr), the SFR increases from about  $3 M_{\odot}/\text{yr}$  to  $10 M_{\odot}/\text{yr}$ .

The middle panels track the accretion rate of the central BH as a fraction of the Eddington rate. Early in the subhalo's history ( $t < 2$  Gyr), the BH experiences high accretion, which steadily declines until  $t \sim 5$  Gyr. Around  $t \sim 3.2$  Gyr, the BH accretion rate peaks again, reaching approximately 30% of the Eddington limit, placing the BH in quasar mode and

injecting significant thermal energy into the galaxy's center. The middle right panel shows the period between  $t = 2$  and  $5$  Gyr.

The lower panel illustrates the growth of the subhalo's virial mass ( $M_{200}$ ). Early on ( $t < 4$  Gyr),  $M_{200}$  increases roughly linearly, reaching about  $2 \times 10^{12} M_{\odot}$ . After this, the mass remains relatively stable until jumps occur around  $t \sim 10$  and  $\sim 12$  Gyr, indicative of mergers. There are no mergers related to the earlier quiescent period around  $t \sim 3.2$  Gyr, as no major mass jumps are observed during this time. The lower right panel shows the period between  $t = 2$  and  $5$  Gyr.

### 3.4. Sequence of Events

Figure 4 presents surface density projections of gas and stars at different stages of the high- to low- $\alpha$  transition. The upper panels show gas density, while the middle panels display stellar density. Time progresses from  $\sim 2.4$  to  $\sim 3.6$  Gyr, corresponding to redshifts ranging from  $z \sim 2.7$  to  $z \sim 1.8$ .

This Figure shows the following sequence of events:



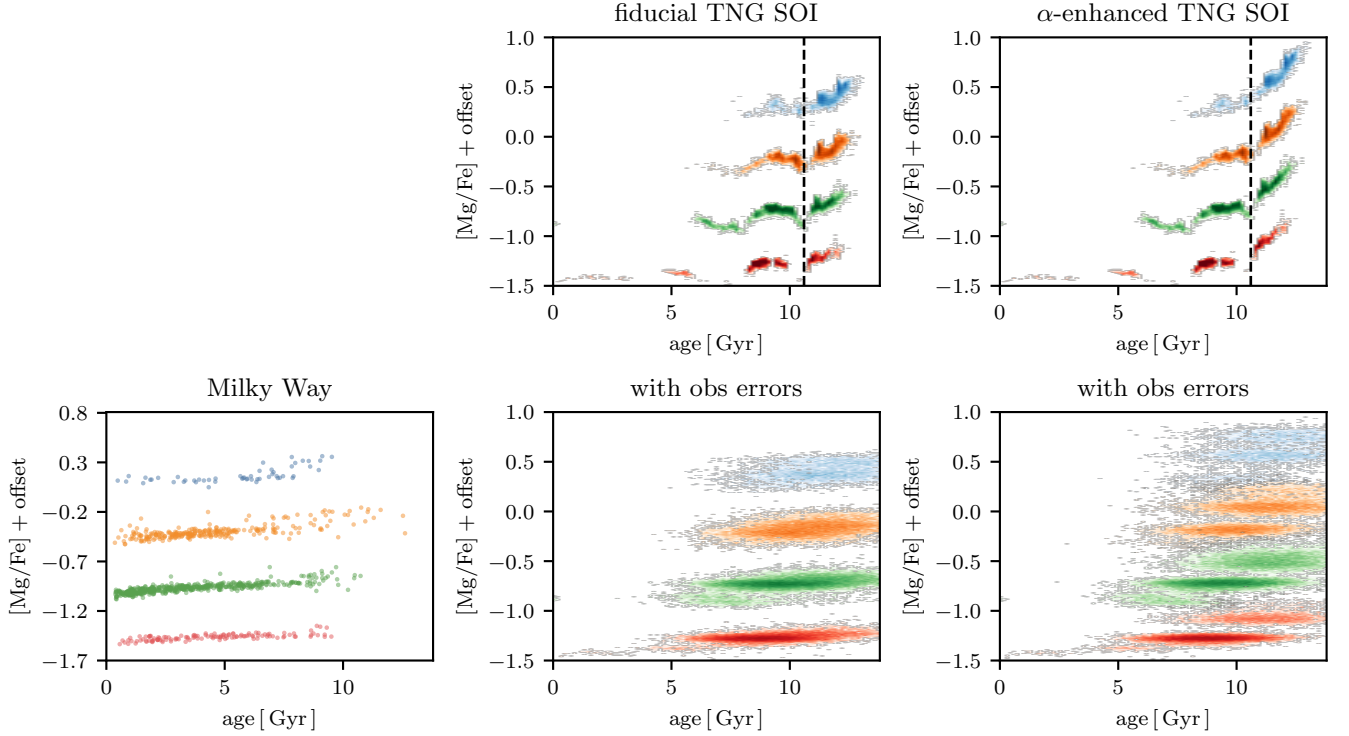


**Figure 2. Bimodality in the abundance plane is linked to distinct epochs in simulation.** The upper panels show  $[\text{Mg}/\text{Fe}]$  as a function of age for our subhalo in TNG. The colors indicate stellar populations at fixed values of  $[\text{Fe}/\text{H}]$ , which are the same as in Figure 1. A gap in the relation occurs at an age of approximately 10.6 Gyr, which we indicate with a vertical dashed line. The effect of the  $\alpha$ -enhancement is clear, as it separates the stars that form before and after this gap in ages (star particles which formed before  $z = 1.5$  are  $\alpha$ -enhanced, which occurs at an age of  $\sim 9.5$  Gyr). The lower panels show on the left the Milky Way and on the center and right the data from TNG but with 15% age errors and 0.01 dex errors in  $[\text{Mg}/\text{Fe}]$ . When the simulations are given these errors, we see that the before and after star particles smear such that the two populations significantly overlap in ages. In the  $\alpha$ -enhanced SOI, two populations emerge in each bin which overlapped in the fiducial distribution. This feature more closely resembles the Milky Way, which displays such populations where the bimodality is strongest –  $[\text{Fe}/\text{H}] = -0.5$  (blue) and  $-0.25$  (orange).

1. Bar forms: A steady increase in the bar strength, as indicated by  $A_2/A_0$  for star particles with  $R < 2$  kpc, from  $\sim 0.05$  to  $0.4$  starting around 2.8 Gyr. This rise is accompanied by the appearance of elongated features in the gas and stars consistent with a bar.
2. BH accretion increases: Following the increase in bar strength by about a snapshot ( $\sim 150$  Myr here), the BH accretion rate ( $\dot{M}_{\text{BH}}/\dot{M}_{\text{edd}}$ ) shows a significant spike, rising from a minimum of  $\sim 0.08$  at  $t = 2.84$  Gyr to a maximum of  $\sim 0.29$  at  $t = 3.13$  Gyr for one snapshot.
3. SFR declines: The SFR declines starting from a maximum of  $54.3 M_{\odot}/\text{yr}$  at  $t = 2.84$  Gyr down to  $3.6 M_{\odot}/\text{yr}$  at  $t = 3.28$  Gyr. In the next snapshot at  $t = 3.45$  Gyr the SFR recovers to  $12.2 M_{\odot}/\text{yr}$  and remains above

After the increase in BH accretion, the star formation rate (SFR) begins to decline. The decrease in SFR steadily commences as the BH accretion rate remains elevated. By approximately 3.2 Gyr, the SFR reaches a

more quiescent state at  $\sim 3 M_{\odot}/\text{yr}$ . After one snapshot, the SFR increases to

### 3.5. One-Zone Model

In Figure 1, we showed that a time-linear  $\alpha$ -enhancement of older stars (formed before  $z = 1.5$ ) leads to the emergence of a pronounced chemical bimodality. This  $\alpha$ -enhancement corresponds to a more rapid decline in  $[\alpha/\text{Fe}]$  over time at high redshifts. Figure 5 demonstrates that having too low SFE at high densities is a plausible explanation for why such a steep decline in  $[\alpha/\text{Fe}]$  might not be occurring in the fiducial TNG model.

The upper panel of Figure 5 presents the evolution of  $[\text{Mg}/\text{Fe}]$  in three one-zone chemical evolution models with varying star formation efficiencies (SFE). A higher SFE leads to a faster reduction in  $[\text{Mg}/\text{Fe}]$ . In the model with the highest SFE ( $2 \text{ Gyr}^{-1}$ , blue, where  $\text{SFE} = \dot{\Sigma}_{\text{star}}/\Sigma_{\text{gas}}$ ),  $[\text{Mg}/\text{Fe}]$  drops from  $\sim 0.45$  to  $0.08$  dex over 2 Gyr. In contrast, the model with the lowest SFE ( $0.2 \text{ Gyr}^{-1}$ ) only reaches  $\sim 0.2$  dex within the same period.

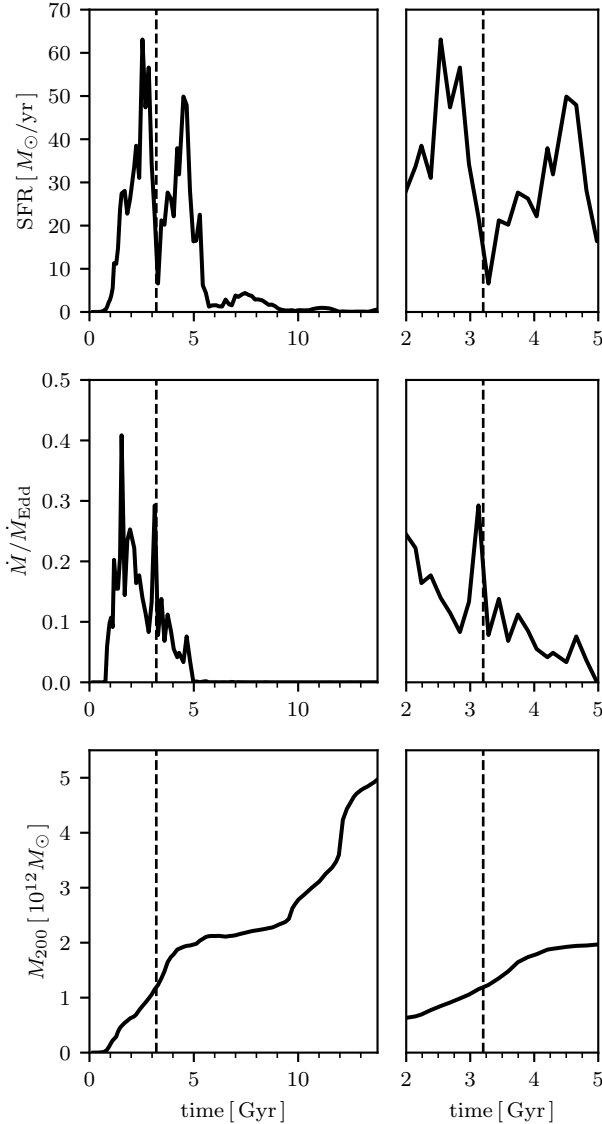


**Figure 3. The evolutionary history of our subhalo of interest.** The left column shows the SFH, BH accretion rate, and virial mass ( $M_{200}$ ) over the entire time span, while the right column zooms in on the period from  $t \sim 2$  Gyr to  $t \sim 5$  Gyr. The vertical dashed line in each panel marks the transition at  $t \sim 3.2$  Gyr, corresponding to the separation between the high- and low- $\alpha$  sequences (as shown in Figure 2). The middle panel shows the BH accretion rate as a fraction of the Eddington limit, and the lower panel shows the virial mass, representing the mass enclosed within a radius where the density is  $200\times$  the mean cosmic density.

The lower panel shows the negative time derivative of  $[\text{Mg}/\text{Fe}]$  (i.e., the rate of decline). The model with the highest SFE ( $2 \text{ Gyr}^{-1}$ , blue) has a peak decline rate of  $-0.5 \text{ dex/Gyr}$ , while the model with the lowest SFE ( $0.2 \text{ Gyr}^{-1}$ ) peaks at  $-0.25 \text{ dex/Gyr}$ . After 1 Gyr, the trend begins to reverse, and the lower-SFE models catch up, though at a much slower rate ( $\sim -0.1 \text{ dex/Gyr}$ ) compared to their peak.

This analysis illustrates that a higher SFE at early times (high redshift) leads to a faster decrease in  $[\text{Mg}/\text{Fe}]$ . Recent work has suggested that the SFE in such dense regions in TNG may indeed be too low, as discussed in Section 4.2.

#### 4. DISCUSSION

In Figure 1, we compared the abundance plane between the Milky Way and our SoI before and after our  $\alpha$ -enhancement post-processing procedure. It is clear that the TNG SoI is unimodal before the  $\alpha$ -enhancement and multi-modal afterwards. Here, we briefly discuss two main points: (1) assuming the  $\alpha$ -enhancement is justified, what leads to the bimodality in the SoI?, and (2) what justifies the  $\alpha$ -enhancement? We then briefly extend our comparison to the Milky Way data.

##### 4.1. Cause of Bimodality

An extensive analysis of our SoI is beyond the scope of this work, but here we argue that the evidence is consistent with the scenario presented in Paper I. They presented an idealized simulation resembling the merger between the Milky Way and GSE. They varied the orbital parameters slightly in a grid of 27 simulations and found that simulations which had a brief quiescent period as a result of the merger led to a bimodal abundance distribution. They argued that AGN activity was responsible for this brief quenching.

Once the  $\alpha$ -enhancement post-processing has been done, the SoI that we have studied in this work is consistent with this scenario. The vertical dashed line in Figures 2 and 3 denotes the transition between the high- and low- $\alpha$  sequences. We place it at a lookback time of 10.6 Gyr or a formation time of  $\sim 3.2$  Gyr. The upper right panel of Figure 2 shows 2D histograms of  $[\text{Mg}/\text{Fe}]$  vs star particle age in fixed bins of  $[\text{Fe}/\text{H}]$  (each color is a different  $[\text{Fe}/\text{H}]$  bin, and an offset is given to  $[\text{Mg}/\text{Fe}]$  so their medians are at zero). Stars formed before the dashed line had a steep decline of  $[\text{Mg}/\text{Fe}]$  with time, while the relation in star particles formed after the dashed line is much more flat. At the line, we see a gap in the  $[\text{Fe}/\text{H}] = -0.5$  and  $-0.25$  bins.

The age gap in each  $[\text{Fe}/\text{H}]$  bin of Figure 2 is contemporaneous with a minimum in the global SFR. We can see in the upper panel of Figure 3 that this dashed line lies almost exactly at the point of a local minimum in the SFH. This minimum, which is  $\sim 3 M_{\odot}/\text{yr}$ , is  $10\text{--}15\times$  smaller than the maxima before and after it.

During this period of suppressed SF, we argue that the lack of enrichment of Type II relative to Type Ia SNe leads to a lower rate of Mg production. Therefore,  $[\text{Mg}/\text{Fe}]$  rapidly declines. This, combined with a lack of SF in the first place, leads to a scarcity of star particles in the intermediate region between the high- and low- $\alpha$  sequences. A more in-depth explanation is given in Section 4.1 in Paper I.

In the fiducial TNG distribution, shown in the upper middle panel of Figure 2, the same general behavior is present.

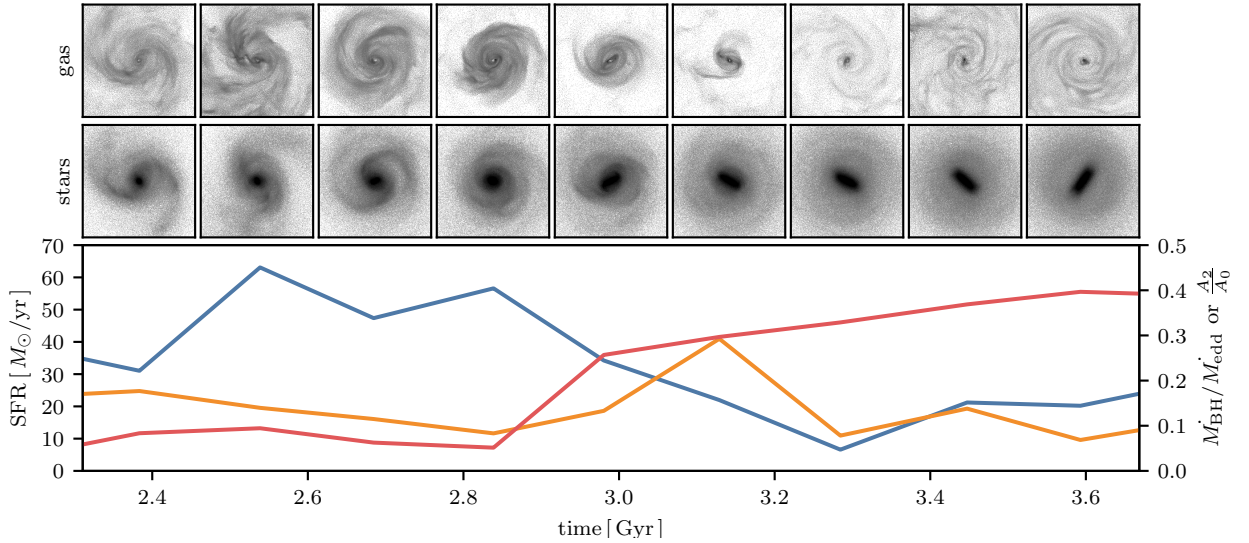


**Figure 4.** Surface density projections of gas (top row) and star particles (middle row) in our SoI across snapshots at different times during the high- to low- $\alpha$  transition. Below the projections is a plot showing the SFR, BH accretion rate (in units of  $\dot{M}_{\text{BH}}/\dot{M}_{\text{edd}}$ ), and bar strength ( $A_2/A_0$  for  $R < 2$  kpc). Time ranges from  $\sim 2.4$  Gyr to  $\sim 3.6$  Gyr, corresponding to redshifts from  $z \sim 2.7$  to  $z \sim 1.8$ . A sequence of events in which the bar strengthens, BH accretion increases, and SFR declines is seen, and is described more fully in the text.

However, because the  $[\text{Mg}/\text{Fe}]$  decline before the quiescent period is slower, star particles which formed before and after this period overlap in the  $[\text{Mg}/\text{Fe}]$  distribution shown in Figure 1.

It is also worth noting that in both the fiducial and  $\alpha$ -enhanced SoI show a slight rebound effect in  $[\text{Mg}/\text{Fe}]$ . The star particles which form directly after the dashed line have a slightly lower  $[\text{Mg}/\text{Fe}]$  than stars which form after. This was also predicted in Figure 9 of Paper I, where it was argued that during the period of suppressed star formation, the  $[\alpha/\text{Fe}]$  ratio of the star-forming gas drops sharply due to the reduced contribution of Type II relative to Type Ia SNe. Later, the  $[\alpha/\text{Fe}]$  of the gas will recover when the SFR also recovers, but there is a brief window when old, low- $\alpha$  stars can form. A similar behavior was seen in the one-zone models with bursty SFHs in Johnson & Weinberg (2020).

#### 4.2. Steepening of $\alpha$ Decline

As described in Section 2.1, we applied a post-processing to the  $[\text{Mg}/\text{Fe}]$  of star particles in the TNG simulation. Specifically, for star particles formed before  $z = 1.5$ , we added to their  $[\text{Mg}/\text{Fe}]$  a value of  $0.1 \times (t_{1.5} - t_{\text{form}})$ , where  $t_{1.5}$  is the age of the universe at  $z = 1.5$  ( $\sim 4.3$  Gyr) and  $t_{\text{form}}$  is the formation time. This post-processed subhalo is presented alongside the fiducial subhalo in the right and middle columns, respectively, of Figures 1 and 2.

The  $[\text{Mg}/\text{Fe}]$  value of star forming gas is the result of a complicated mixture of many different aspects of the TNG model, to name a few: stellar and AGN feedback which alter gas inflows and outflows, secular, dynamical evolution,

SF prescription, magnetic fields, (lack of) cosmic rays, diffusivity of hydrodynamics solver, and, of course, enrichment models. Isolating the cause of the “incorrect”<sup>2</sup>  $[\text{Mg}/\text{Fe}]$  vs time evolution at high- $z$  is not straightforward nor, in our opinion, even possible. However, we do offer one reasonable explanation: the SFE at high densities, more present at high- $z$ , is too low.

We demonstrate the impact of the SFE on the  $[\alpha/\text{Fe}]$  ratio using a simple one-zone chemical evolution model with the publicly available code VICE. The details of our setup is given in Section 2.3. We vary the SFE of the model ( $\Sigma_{\text{star}}/\Sigma_{\text{gas}}$ ), and examine the impact on the  $[\text{Mg}/\text{Fe}]$  ratio as a function of time. We find that shorter SF timescales do lead to a more rapid reduction in  $[\text{Mg}/\text{Fe}]$ . The rate of decrease in  $[\text{Mg}/\text{Fe}]$ , at its maximum, varies between  $\sim -0.25$ ,  $-0.35$ , and  $-0.5$  dex/Gyr in the SFE = 0.2, 1, and 2 Gyr<sup>-1</sup> models, respectively. For our post-processing, we assumed an additional decrease rate of 0.1 dex/Gyr. Such a difference is well within the range of  $[\text{Mg}/\text{Fe}]$  decrease seen in our different  $\tau_{\star}$  models, implying a factor of only  $\sim 2$  in the SFE is needed to reach our post-processing slope.

Hassan et al. (2024) demonstrated that the pressure regulated feedback model of Ostriker & Kim (2022) predicts higher SFRs of patches of gaseous disks in TNG50 than the fiducial model by up to an order of magnitude. This is well

<sup>2</sup> Our case study of a single subhalo, selected in a non-reproducible manner, is hardly cause to firmly assert that the fiducial evolution in TNG50 is incorrect.

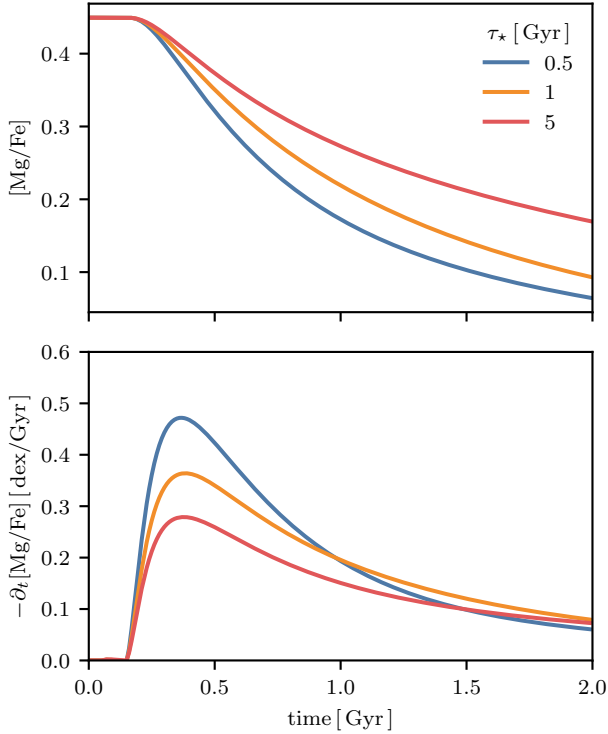


**Figure 5. A higher star formation efficiency leads to a steeper decline in  $[\text{Mg}/\text{Fe}]$ .** In both panels, the lines show the time evolution of  $[\text{Mg}/\text{Fe}]$  in a simple one-zone chemical evolution model, described in Section 2.3. The evolution for different SFE values of 2, 1, and 0.2  $\text{Gyr}^{-1}$  are shown in blue, orange, and red, respectively. The upper panel shows the evolution of  $[\text{Mg}/\text{Fe}]$  over 2 Gyr, while the lower panel shows the negative of its time derivative. Increasing the SFE ( $\Sigma_{\text{star}}/\Sigma_{\text{gas}}$ ) leads to a more rapid decline in  $[\text{Mg}/\text{Fe}]$ . At its steepest decline ( $t \sim 0.5$  Gyr), increasing the SFE by an order of magnitude results in a slope nearly twice as steep. At later times ( $t > 1$  Gyr), models with higher SFE reach their steady-state  $[\text{Mg}/\text{Fe}]$  value more quickly.

within our needed factor of 2 in the SFE (see Figure 5). Therefore,  $[\text{Mg}/\text{Fe}]$  should decline more rapidly with a different feedback model (or future iteration of the TNG model) that leads to a higher SFE at high densities.

An intuitive understanding of the impact the decline in  $[\alpha/\text{Fe}]$  vs time has is that, when  $[\alpha/\text{Fe}]$  declines rapidly, it is a better estimator of age. When  $[\alpha/\text{Fe}]$  is a better estimator of age, events which are separated temporally become better separated in the abundance plane.

#### 4.3. Direct Comparison to Observations

The lower left panel of Figure 2 shows the  $[\text{Mg}/\text{Fe}]$  vs age of stars in bins of  $[\text{Fe}/\text{H}]$  which pass our solar neighborhood selection and are present in the APOKASC2 catalog. In the bins where the bimodality is strongest (blue and orange,  $[\text{Fe}/\text{H}] = -0.5$  and  $-0.25$ , respectively), we see that there is a sort of two tiered distribution with significant overlap in

age. In the SoI with age and abundance errors shown in the lower right panel, a very similar distribution can be seen in all  $[\text{Fe}/\text{H}]$  bins. An examination of the true distribution in the SoI (upper right panel), we see that the two distributions are in fact very cleanly separated in age. We do not know the true underlying distribution in the Milky Way, but these panels show that the general picture shown in our SoI is consistent with the Milky Way.

#### 4.4. Cause of Quiescence

It is natural to question why the minimum in the SFR occurs. In Paper I, AGN activity from a merger was the suspected cause. Here, we can see that there is indeed a brief burst in AGN accretion at the time of the merger (middle panel of Figure 3). Based on this burst, it is reasonable to suspect that AGN activity is also responsible for the quiescent period in our SoI. However, we argue that the cause of the localized spike in the BH accretion rate is not due to a merger but instead due to the formation/strengthening of a bar.

In Figure 4, we combine a visual inspection of the gas (upper row) and stellar (middle row) surface densities with the evolution of three key quantities (lower plot): SFR, BH accretion rate, and bar strength in blue, orange, and red, respectively. These are shown for nine snapshots, from snapshot 27 to 35, corresponding to redshift 2.73 to 1.82 or cosmic time from 2.38 Gyr to 3.59 Gyr. A vertical dashed line is included in the lower panel separating the formation of the low- and high- $\alpha$  sequence at an age of 10.6 Gyr (cosmic time  $\sim 3.2$  Gyr), as in Figures 2 and 3.

As described in Section 3.4, the following sequence of events occurs: the bar strengthens and then the BH accretion rate spikes, all while the SFR of the galaxy declines. This is suggestive of the following causal sequence:

1. a bar forms through an internal instability, which
2. drives a large amount of gas to the center of the galaxy, which
3. triggers a high BH accretion rate and quasar-mode thermal feedback, which
4. clears gas out of the galaxy leading to quiescence.

This quiescent period then leads to the bimodality, as discussed in Section 4.1. It is not possible to prove the causality of this sequence of events because of the sparse snapshot spacing in TNG50, and so this is left to future work.

However, there is a significant body of theoretical and observational work in support of this picture. Bars and other non-axisymmetric features have long been argued to funnel gas into the centers of galaxies on theoretical grounds (Shlosman et al. 1989; Hopkins & Quataert 2010). In observations, barred galaxies preferentially host AGN in star-forming galaxies (Oh et al. 2012; Silva-Lima et al. 2022). Furthermore, at



high- $z$ , the AGN mechanism is thought to be responsible for quenching (e.g. D'Eugenio et al. 2023; Park et al. 2024; Mićić et al. 2024; Belli et al. 2024, and references therein).

Since barred galaxies preferentially host AGN, we therefore predict that barred galaxies would preferentially host  $\alpha$ -bimodalities. The GECKOS survey, which aims to constrain the  $\alpha$ -bimodality of edge-on galaxies using integral field spectroscopy at different altitudes, could test this (van de Sande et al. 2024). On the other hand, the strength of a bar is not associated with the strength of the host AGN (Silva-Lima et al. 2022, e.g.). So, it is not clear that bimodalities would be associated with bar strength.

A complicating factor for this picture comes from the high SFR associated with the galaxy. The depletion time ( $M_{\text{gas}}/\text{SFR}$ ) at the  $t = 2.84$  Gyr snapshot is 204 Myr, shorter than the time it takes for the SFR to reach its minimum. This implies the possibility of starvation as a quenching mechanism. However, the average depletion time in the preceding 5 snapshots (which are each  $\sim 150$  Myr apart) is 220 Myr, so clearly the SoI is accreting high amounts of gas from its CGM. A definitive account, difficult with the current simulation outputs because of its sparse snapshot spacing, requires further work.

## 5. CONCLUSIONS

In this work, we examined a specific subhalo in Illustris TNG50. This subhalo is at a Milky Way-progenitor mass at high- $z$  ( $z \sim 2$ ). After applying a post-processing step that increased the  $[\text{Mg}/\text{Fe}]$  of star particles formed before  $z = 1.5$ , this subhalo hosts a strong bimodality in the plane of  $[\text{Mg}/\text{Fe}]$  and  $[\text{Fe}/\text{H}]$ , shown in Figure 1. This post-processing is justified by arguing that the SFE of dense gas is too low in TNG (Hassan et al. 2024, see discussion in Section 4.2).

This bimodality can be traced to an event that occurred at an age of 10.6 Gyr, or formation time of  $\sim 3.2$  Gyr ( $z \sim 2$ ). Shown as a vertical dashed line in Figure 2, star particles which form before this form at high- $\alpha$  while stars which form after form at lower  $\alpha$ . At the dashed line, there is a gap. We argue that the presence of this gap is responsible for the valley

in the bimodality (Figure 1). It is accompanied by a global reduction in the SFR by about a factor of 6 (upper panel of Figure 3).

This bimodality can be traced to an event that occurred at an age of 10.6 Gyr, or formation time of  $\sim 3.2$  Gyr ( $z \sim 2$ ). Shown as a vertical dashed line in Figure 2, star particles that form before this time are at high- $[\text{Mg}/\text{Fe}]$ , while star particles that form after are at low- $[\text{Mg}/\text{Fe}]$ . This time is associated with a global reduction in the SFR (Figure 3), which appears to be related to AGN activity induced by the formation of a bar (Figure 4).

We argue that the reduction in the SFR has two effects which lead to the  $\alpha$ -bimodality. First, a lower production of Mg relative to Fe is the natural result of a lack of Type II relative to Type Ia SNe. The latter remain high due to their longer timescales, expediting a drop in  $[\text{Mg}/\text{Fe}]$ . Second, the lack of SF means that stars at  $[\text{Mg}/\text{Fe}]$  intermediate between the high- and low- $\alpha$  sequences never form. This argument is the same as presented in Paper I and is consistent with the one-zone chemical evolution models of Johnson & Weinberg (2020). When observational errors are added to the subhalo's abundance vs age distribution, we show that it is broadly consistent with the distribution observed in the Milky Way (Figure 2 and Section 4.3).

This work adds further support to a scenario in which a quiescent period in the Milky Way's past is a plausible explanation for the Milky Way's abundance bimodality. We argued in Paper I that the GSE merger could trigger this period. In this work we have argued that the formation of the Milky Way's bar could be responsible. In external galaxies, we predict that the presence of a bar is correlated with the presence of an  $\alpha$ -bimodality.

- 1 This work has made use of data from the European Space
- 2 Agency (ESA) mission *Gaia* (<https://www.cosmos.esa.int/gaia>), processed by the *Gaia* Data Processing and Anal-
- 3 ysis Consortium (DPAC, <https://www.cosmos.esa.int/web/gaia/dpac/consortium>). Funding for the DPAC has been pro-
- 4 vided by national institutions, in particular the institutions
- 5 participating in the *Gaia* Multilateral Agreement.

## REFERENCES

- Adibekyan, V. Z., Santos, N. C., Sousa, S. G., & Israelian, G. 2011, A&A, 535, L11, doi: [10.1051/0004-6361/201118240](https://doi.org/10.1051/0004-6361/201118240)
- Adibekyan, V. Z., Sousa, S. G., Santos, N. C., et al. 2012, A&A, 545, A32, doi: [10.1051/0004-6361/201219401](https://doi.org/10.1051/0004-6361/201219401)
- Beane, A. 2024, arXiv e-prints, arXiv:2407.07985, doi: [10.48550/arXiv.2407.07985](https://doi.org/10.48550/arXiv.2407.07985)
- Belli, S., Park, M., Davies, R. L., et al. 2024, Nature, 630, 54, doi: [10.1038/s41586-024-07412-1](https://doi.org/10.1038/s41586-024-07412-1)
- Belokurov, V., Erkal, D., Evans, N. W., Koposov, S. E., & Deason, A. J. 2018, MNRAS, 478, 611, doi: [10.1093/mnras/sty982](https://doi.org/10.1093/mnras/sty982)
- Bensby, T., Feltzing, S., & Oey, M. S. 2014, A&A, 562, A71, doi: [10.1051/0004-6361/201322631](https://doi.org/10.1051/0004-6361/201322631)
- Beraldo e Silva, L., Debattista, V. P., Khachatryan, T., & Nidever, D. 2020, MNRAS, 492, 4716, doi: [10.1093/mnras/staa065](https://doi.org/10.1093/mnras/staa065)

- Beraldo e Silva, L., Debattista, V. P., Nidever, D., Amarante, J. A. S., & Garver, B. 2021, MNRAS, 502, 260, doi: [10.1093/mnras/staa3966](https://doi.org/10.1093/mnras/staa3966)
- Bland-Hawthorn, J., & Gerhard, O. 2016, ARA&A, 54, 529, doi: [10.1146/annurev-astro-081915-023441](https://doi.org/10.1146/annurev-astro-081915-023441)
- Bondi, H. 1952, MNRAS, 112, 195, doi: [10.1093/mnras/112.2.195](https://doi.org/10.1093/mnras/112.2.195)
- Bondi, H., & Hoyle, F. 1944, MNRAS, 104, 273, doi: [10.1093/mnras/104.5.273](https://doi.org/10.1093/mnras/104.5.273)
- Brook, C., Richard, S., Kawata, D., Martel, H., & Gibson, B. K. 2007, ApJ, 658, 60, doi: [10.1086/511056](https://doi.org/10.1086/511056)
- Brook, C. B., Gibson, B. K., Martel, H., & Kawata, D. 2005, ApJ, 630, 298, doi: [10.1086/431924](https://doi.org/10.1086/431924)
- Brook, C. B., Kawata, D., Gibson, B. K., & Freeman, K. C. 2004, ApJ, 612, 894, doi: [10.1086/422709](https://doi.org/10.1086/422709)
- Buck, T. 2020, MNRAS, 491, 5435, doi: [10.1093/mnras/stz3289](https://doi.org/10.1093/mnras/stz3289)
- Chandra, V., Semenov, V. A., Rix, H.-W., et al. 2024, ApJ, 972, 112, doi: [10.3847/1538-4357/ad5b60](https://doi.org/10.3847/1538-4357/ad5b60)
- Chen, B., Hayden, M. R., Sharma, S., et al. 2023, MNRAS, 523, 3791, doi: [10.1093/mnras/stad1568](https://doi.org/10.1093/mnras/stad1568)
- Chiappini, C. 2009, in The Galaxy Disk in Cosmological Context, ed. J. Andersen, Nordströara, B. m, & J. Bland-Hawthorn, Vol. 254, 191–196, doi: [10.1017/S1743921308027580](https://doi.org/10.1017/S1743921308027580)
- Chiappini, C., Matteucci, F., & Gratton, R. 1997, ApJ, 477, 765, doi: [10.1086/303726](https://doi.org/10.1086/303726)
- Ciucă, I., Kawata, D., Ting, Y.-S., et al. 2024, MNRAS, 528, L122, doi: [10.1093/mnrasl/slad033](https://doi.org/10.1093/mnrasl/slad033)
- Clarke, A. J., Debattista, V. P., Nidever, D. L., et al. 2019, MNRAS, 484, 3476, doi: [10.1093/mnras/stz104](https://doi.org/10.1093/mnras/stz104)
- D'Eugenio, F., Perez-Gonzalez, P., Maiolino, R., et al. 2023, arXiv e-prints, arXiv:2308.06317, doi: [10.48550/arXiv.2308.06317](https://doi.org/10.48550/arXiv.2308.06317)
- Fuhrmann, K. 1998, A&A, 338, 161
- . 2004, Astronomische Nachrichten, 325, 3, doi: [10.1002/asna.200310173](https://doi.org/10.1002/asna.200310173)
- García Pérez, A. E., Allende Prieto, C., Holtzman, J. A., et al. 2016, AJ, 151, 144, doi: [10.3847/0004-6256/151/6/144](https://doi.org/10.3847/0004-6256/151/6/144)
- Garver, B. R., Nidever, D. L., Debattista, V. P., Beraldo e Silva, L., & Khachatryan, T. 2023, ApJ, 953, 128, doi: [10.3847/1538-4357/acdfc6](https://doi.org/10.3847/1538-4357/acdfc6)
- Gratton, R., Carretta, E., Matteucci, F., & Sneden, C. 1996, in Astronomical Society of the Pacific Conference Series, Vol. 92, Formation of the Galactic Halo...Inside and Out, ed. H. L. Morrison & A. Sarajedini, 307
- Grisoni, V., Spitoni, E., Matteucci, F., et al. 2017, MNRAS, 472, 3637, doi: [10.1093/mnras/stx2201](https://doi.org/10.1093/mnras/stx2201)
- Hassan, S., Ostriker, E. C., Kim, C.-G., et al. 2024, arXiv e-prints, arXiv:2409.09121, doi: [10.48550/arXiv.2409.09121](https://doi.org/10.48550/arXiv.2409.09121)
- Hayden, M. R., Bland-Hawthorn, J., Sharma, S., et al. 2020, MNRAS, 493, 2952, doi: [10.1093/mnras/staa335](https://doi.org/10.1093/mnras/staa335)
- Helmi, A., Babusiaux, C., Koppelman, H. H., et al. 2018, Nature, 563, 85, doi: [10.1038/s41586-018-0625-x](https://doi.org/10.1038/s41586-018-0625-x)
- Hopkins, P. F., & Quataert, E. 2010, MNRAS, 407, 1529, doi: [10.1111/j.1365-2966.2010.17064.x](https://doi.org/10.1111/j.1365-2966.2010.17064.x)
- Hoyle, F., & Lyttleton, R. A. 1939, Proceedings of the Cambridge Philosophical Society, 35, 405, doi: [10.1017/S0305004100021150](https://doi.org/10.1017/S0305004100021150)
- Johnson, J. W., & Weinberg, D. H. 2020, MNRAS, 498, 1364, doi: [10.1093/mnras/staa2431](https://doi.org/10.1093/mnras/staa2431)
- Khoperskov, S., Haywood, M., Snaith, O., et al. 2021, MNRAS, 501, 5176, doi: [10.1093/mnras/staa3996](https://doi.org/10.1093/mnras/staa3996)
- Mićić, M., Irwin, J. A., Nair, P., et al. 2024, arXiv e-prints, arXiv:2405.18685, <https://arxiv.org/abs/2405.18685>
- Naidu, R. P., Conroy, C., Bonaca, A., et al. 2020, ApJ, 901, 48, doi: [10.3847/1538-4357/abaf4](https://doi.org/10.3847/1538-4357/abaf4)
- Nelson, D., Pillepich, A., Springel, V., et al. 2019, MNRAS, 490, 3234, doi: [10.1093/mnras/stz2306](https://doi.org/10.1093/mnras/stz2306)
- Nidever, D. L., Bovy, J., Bird, J. C., et al. 2014, ApJ, 796, 38, doi: [10.1088/0004-637X/796/1/38](https://doi.org/10.1088/0004-637X/796/1/38)
- Oh, S., Oh, K., & Yi, S. K. 2012, ApJS, 198, 4, doi: [10.1088/0067-0049/198/1/4](https://doi.org/10.1088/0067-0049/198/1/4)
- Ostriker, E. C., & Kim, C.-G. 2022, ApJ, 936, 137, doi: [10.3847/1538-4357/ac7de2](https://doi.org/10.3847/1538-4357/ac7de2)
- Pakmor, R., Springel, V., Bauer, A., et al. 2016, MNRAS, 455, 1134, doi: [10.1093/mnras/stv2380](https://doi.org/10.1093/mnras/stv2380)
- Park, M., Belli, S., Conroy, C., et al. 2024, arXiv e-prints, arXiv:2404.17945, doi: [10.48550/arXiv.2404.17945](https://doi.org/10.48550/arXiv.2404.17945)
- Pillepich, A., Springel, V., Nelson, D., et al. 2018, MNRAS, 473, 4077, doi: [10.1093/mnras/stx2656](https://doi.org/10.1093/mnras/stx2656)
- Pillepich, A., Nelson, D., Springel, V., et al. 2019, MNRAS, 490, 3196, doi: [10.1093/mnras/stz2338](https://doi.org/10.1093/mnras/stz2338)
- Pinsonneault, M. H., Elsworth, Y. P., Tayar, J., et al. 2018, ApJS, 239, 32, doi: [10.3847/1538-4365/aaebfd](https://doi.org/10.3847/1538-4365/aaebfd)
- Reddy, B. E., Lambert, D. L., & Allende Prieto, C. 2006, MNRAS, 367, 1329, doi: [10.1111/j.1365-2966.2006.10148.x](https://doi.org/10.1111/j.1365-2966.2006.10148.x)
- Richard, S., Brook, C. B., Martel, H., et al. 2010, MNRAS, 402, 1489, doi: [10.1111/j.1365-2966.2009.16008.x](https://doi.org/10.1111/j.1365-2966.2009.16008.x)
- Schönrich, R., & Binney, J. 2009, MNRAS, 396, 203, doi: [10.1111/j.1365-2966.2009.14750.x](https://doi.org/10.1111/j.1365-2966.2009.14750.x)
- Sharma, S., Hayden, M. R., & Bland-Hawthorn, J. 2021, MNRAS, 507, 5882, doi: [10.1093/mnras/stab2015](https://doi.org/10.1093/mnras/stab2015)
- Shlosman, I., Frank, J., & Begelman, M. C. 1989, Nature, 338, 45, doi: [10.1038/338045a0](https://doi.org/10.1038/338045a0)
- Silva-Lima, L. A., Martins, L. P., Coelho, P. R. T., & Gadotti, D. A. 2022, A&A, 661, A105, doi: [10.1051/0004-6361/202142432](https://doi.org/10.1051/0004-6361/202142432)
- Spitoni, E., Matteucci, F., Gratton, R., et al. 2024, arXiv e-prints, arXiv:2405.11025, doi: [10.48550/arXiv.2405.11025](https://doi.org/10.48550/arXiv.2405.11025)
- Spitoni, E., Silva Aguirre, V., Matteucci, F., Calura, F., & Grisoni, V. 2019, A&A, 623, A60, doi: [10.1051/0004-6361/201834188](https://doi.org/10.1051/0004-6361/201834188)
- Springel, V. 2010, MNRAS, 401, 791, doi: [10.1111/j.1365-2966.2009.15715.x](https://doi.org/10.1111/j.1365-2966.2009.15715.x)

- van de Sande, J., Fraser-McKelvie, A., Fisher, D. B., et al. 2024, in IAU Symposium, Vol. 377, Early Disk-Galaxy Formation from JWST to the Milky Way, ed. F. Tabatabaei, B. Barbuy, & Y.-S. Ting, 27–33, doi: [10.1017/S1743921323001138](https://doi.org/10.1017/S1743921323001138)
- van Dokkum, P. G., Leja, J., Nelson, E. J., et al. 2013, ApJL, 771, L35, doi: [10.1088/2041-8205/771/2/L35](https://doi.org/10.1088/2041-8205/771/2/L35)
- Vogelsberger, M., Genel, S., Sijacki, D., et al. 2013, MNRAS, 436, 3031, doi: [10.1093/mnras/stt1789](https://doi.org/10.1093/mnras/stt1789)
- Weinberger, R., Springel, V., Hernquist, L., et al. 2017, MNRAS, 465, 3291, doi: [10.1093/mnras/stw2944](https://doi.org/10.1093/mnras/stw2944)

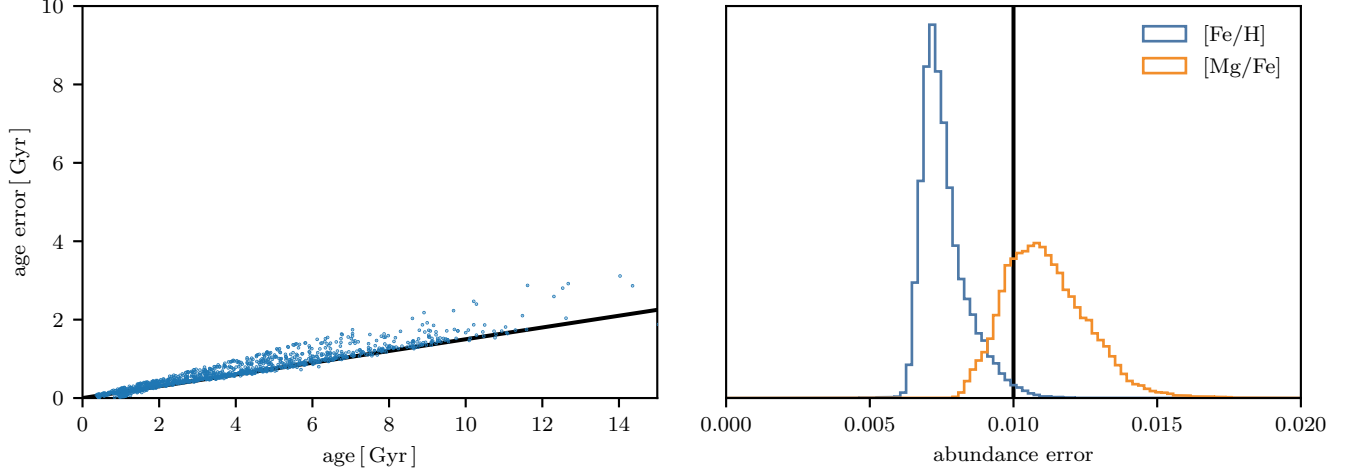


**Figure 6.** The observational errors of the APOKASC2 (left) and ASPCAP dataset (right). We show, on the left, a line indicating a 15% error in observed age and on the right a vertical line indicating a 0.01 dex error.

## APPENDIX

### A. OBSERVATIONAL ERRORS

In Figure 2, we assumed observational errors of 15% in age and 0.01 dex in  $[\text{Mg}/\text{Fe}]$ . In Figure 6, we plot the quoted observational errors of the APOKASC2 (left) and ASPCAP (right) datasets, showing both  $[\text{Fe}/\text{H}]$  and  $[\text{Mg}/\text{Fe}]$  (blue and orange, respectively). We show our 15% age error and 0.01 dex abundance error assumptions as black lines. For the age error, we used the maximum of the upper and lower estimates from Pinsonneault et al. (2018). Our assumed errors are generally consistent with the errors. Our error in  $[\text{Mg}/\text{Fe}]$  is a bit smaller than in ASPCAP, but the age estimates are by far the more constraining of the two.

### B. RANDOM SELECTION OF SUBHALOS

In Figures 7 to 23, we show a version of Figure 1 but for a random selection of subhalos from our broader sample of 168 Milky Way-progenitors at  $z = 1.5$  in TNG50. It is from this sample that we selected our SoI. We first show our SoI at  $z = 1.5$  in Figure 7, and then show our random sample of 16.



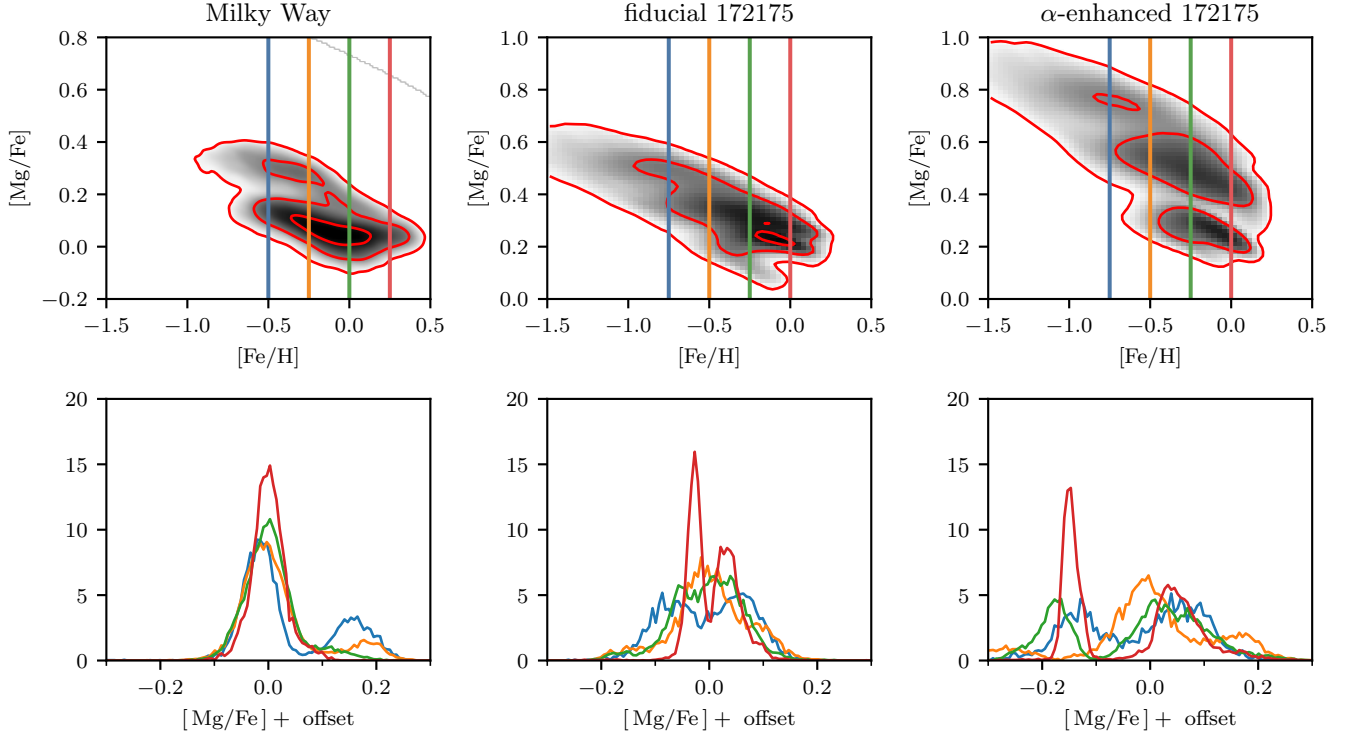


**Figure 7.** The same as Figure 1, but for our SoI at  $z = 1.5$ .

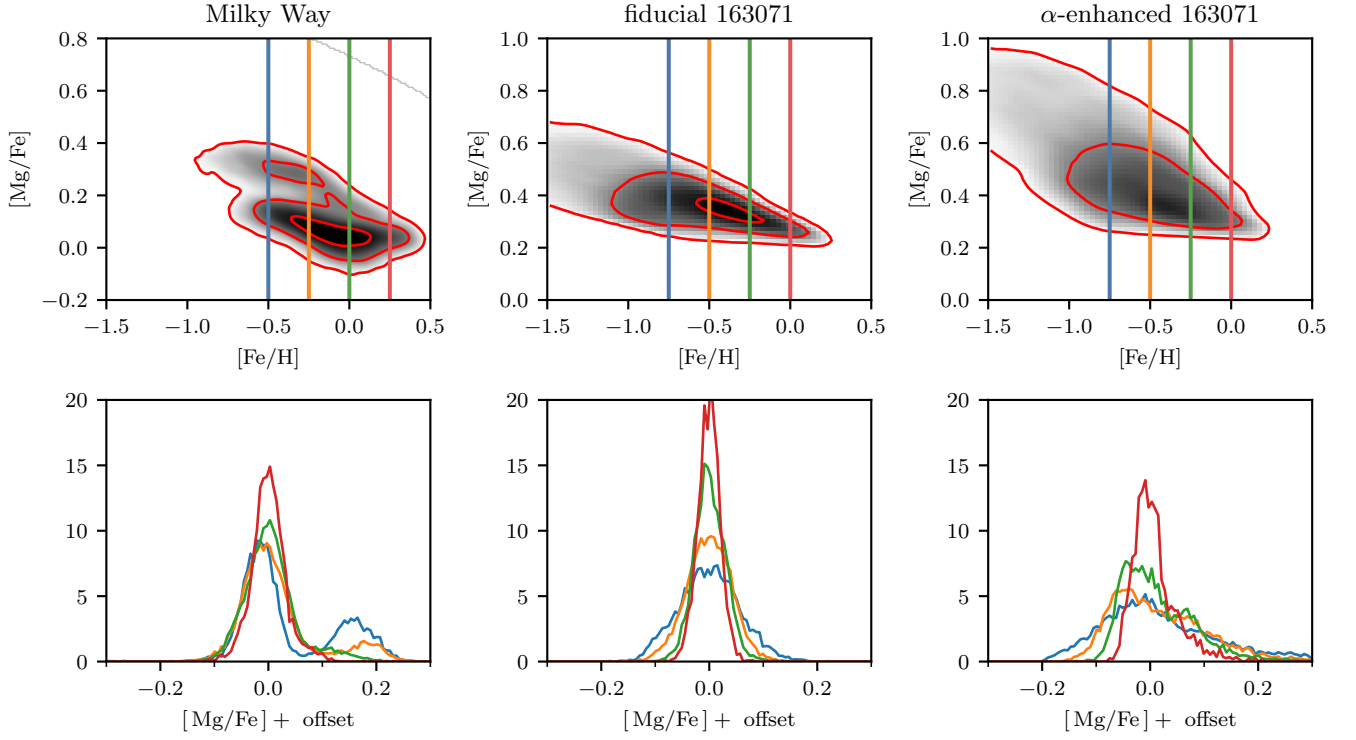


**Figure 8.** The same as Figure 1, but for a random subhalo from our catalog at  $z = 1.5$ .

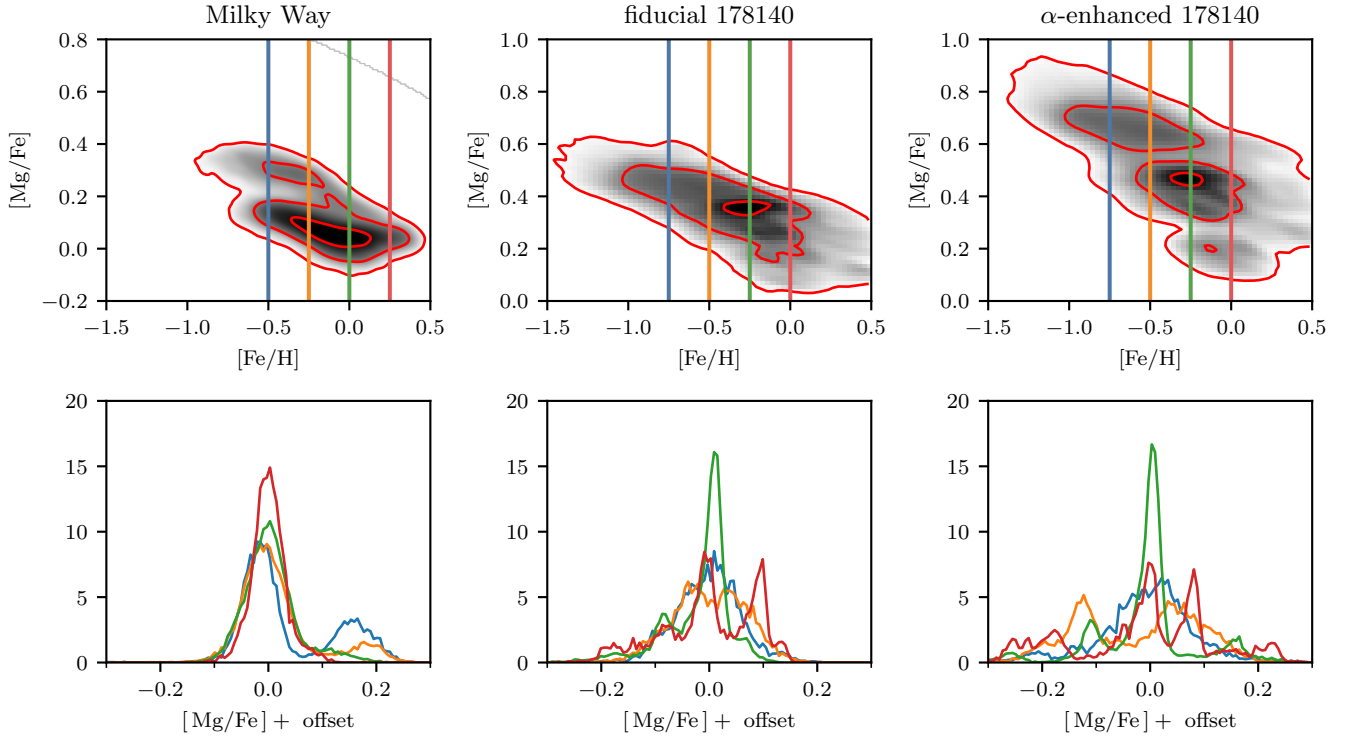


**Figure 9.** The same as Figure 1, but for a random subhalo from our catalog at  $z = 1.5$ .

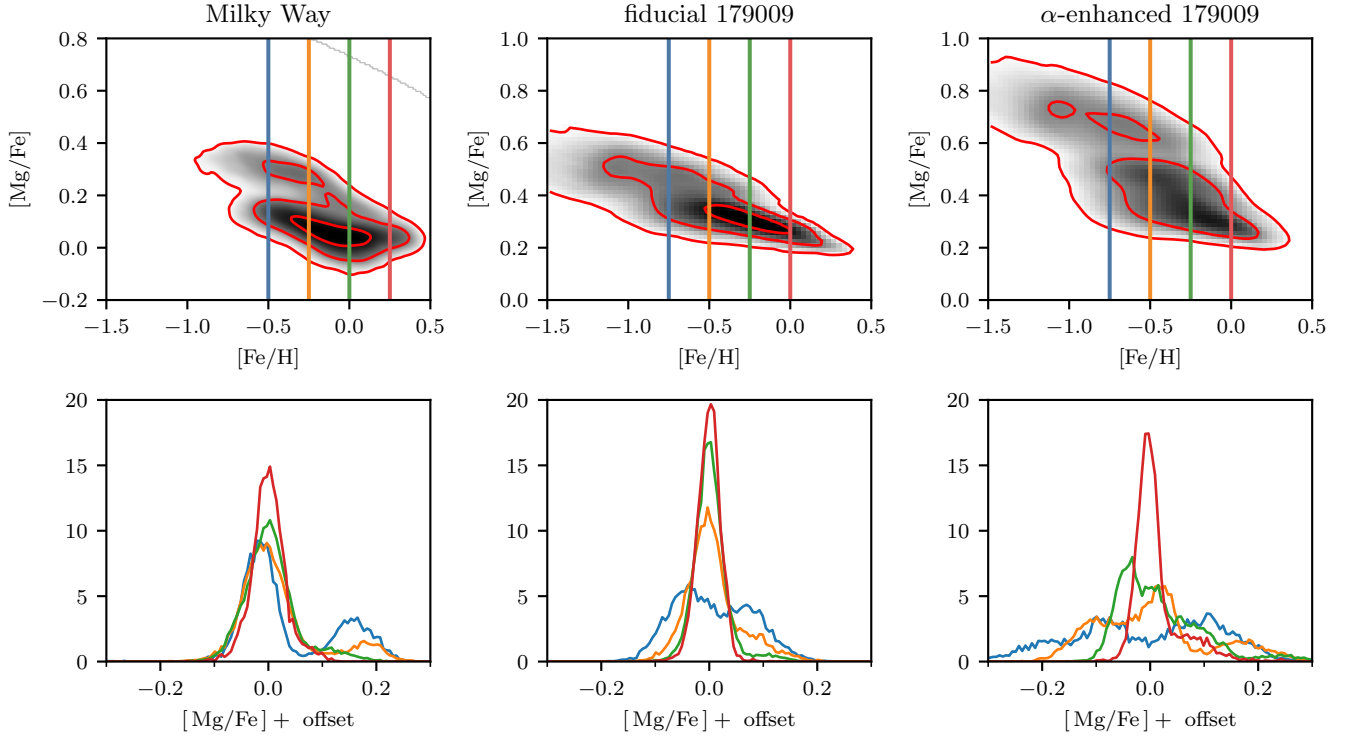


**Figure 10.** The same as Figure 1, but for a random subhalo from our catalog at  $z = 1.5$ .

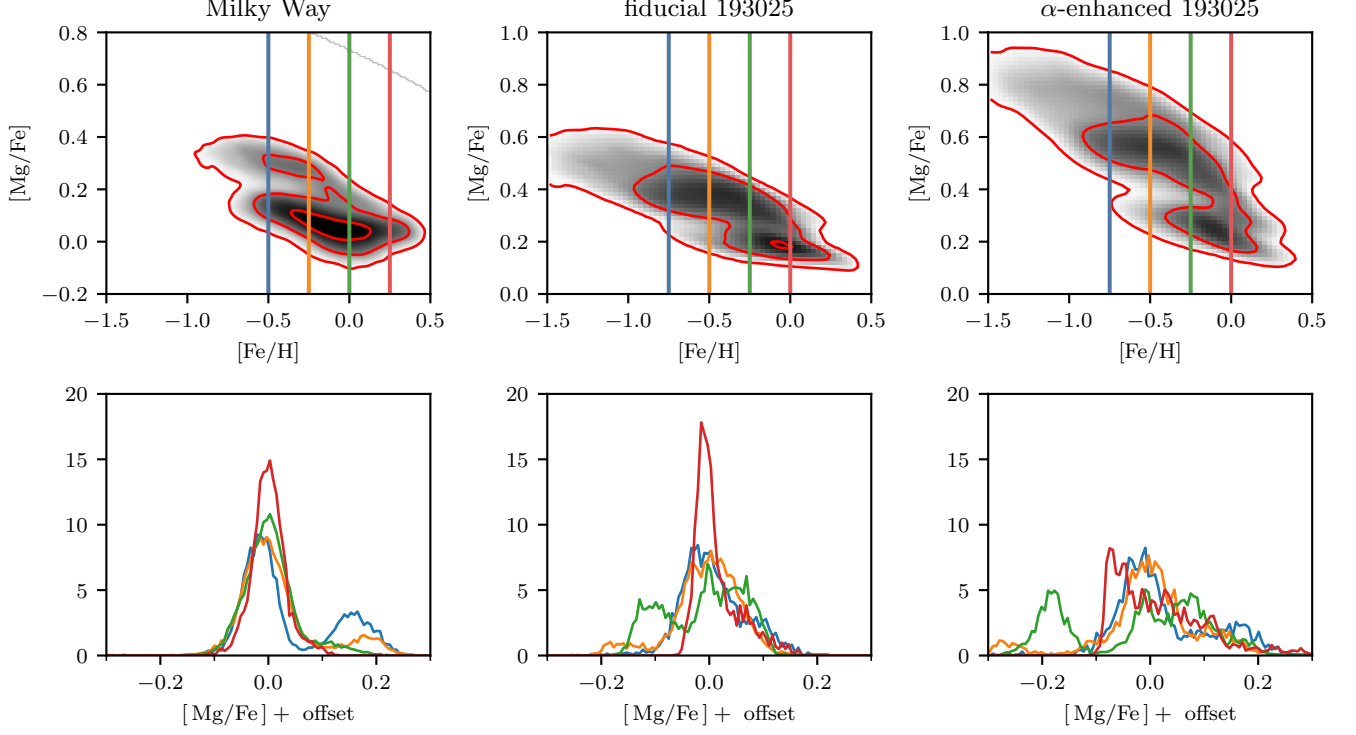


**Figure 11.** The same as Figure 1, but for a random subhalo from our catalog at  $z = 1.5$ .

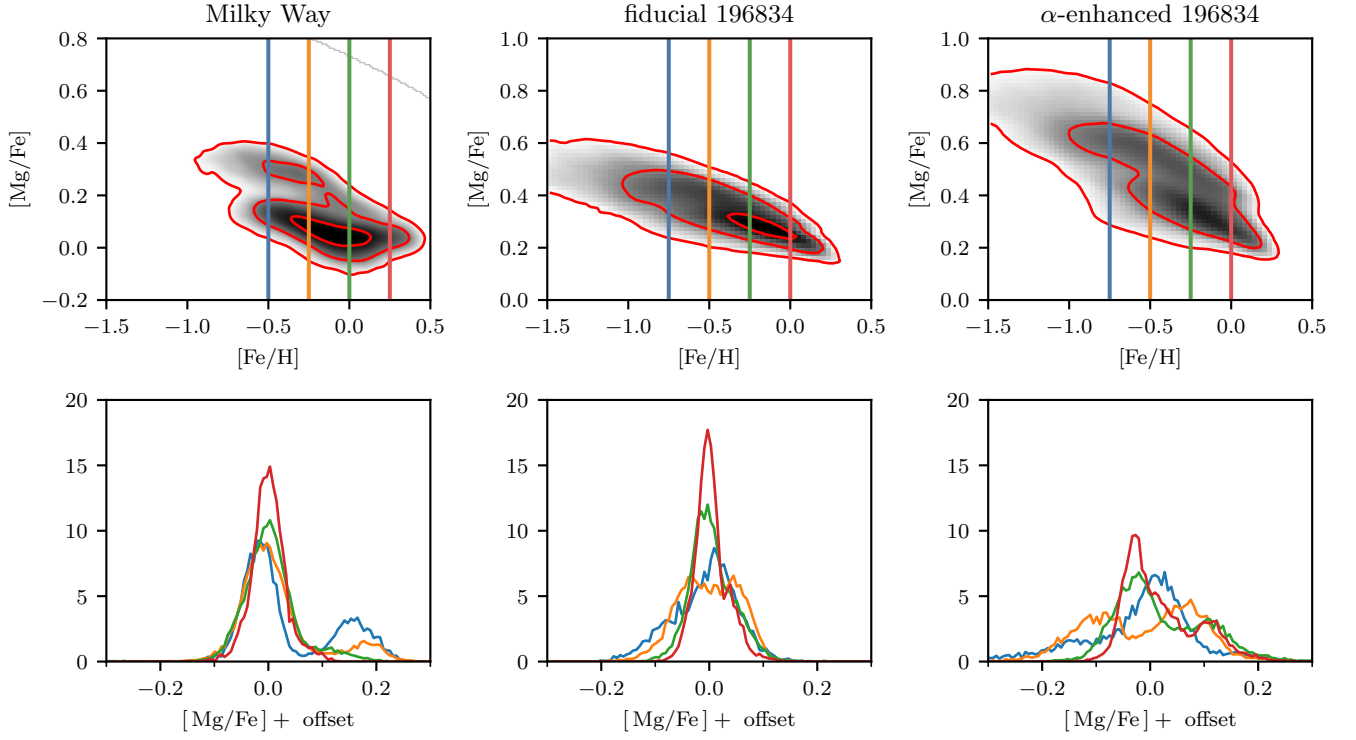


**Figure 12.** The same as Figure 1, but for a random subhalo from our catalog at  $z = 1.5$ .

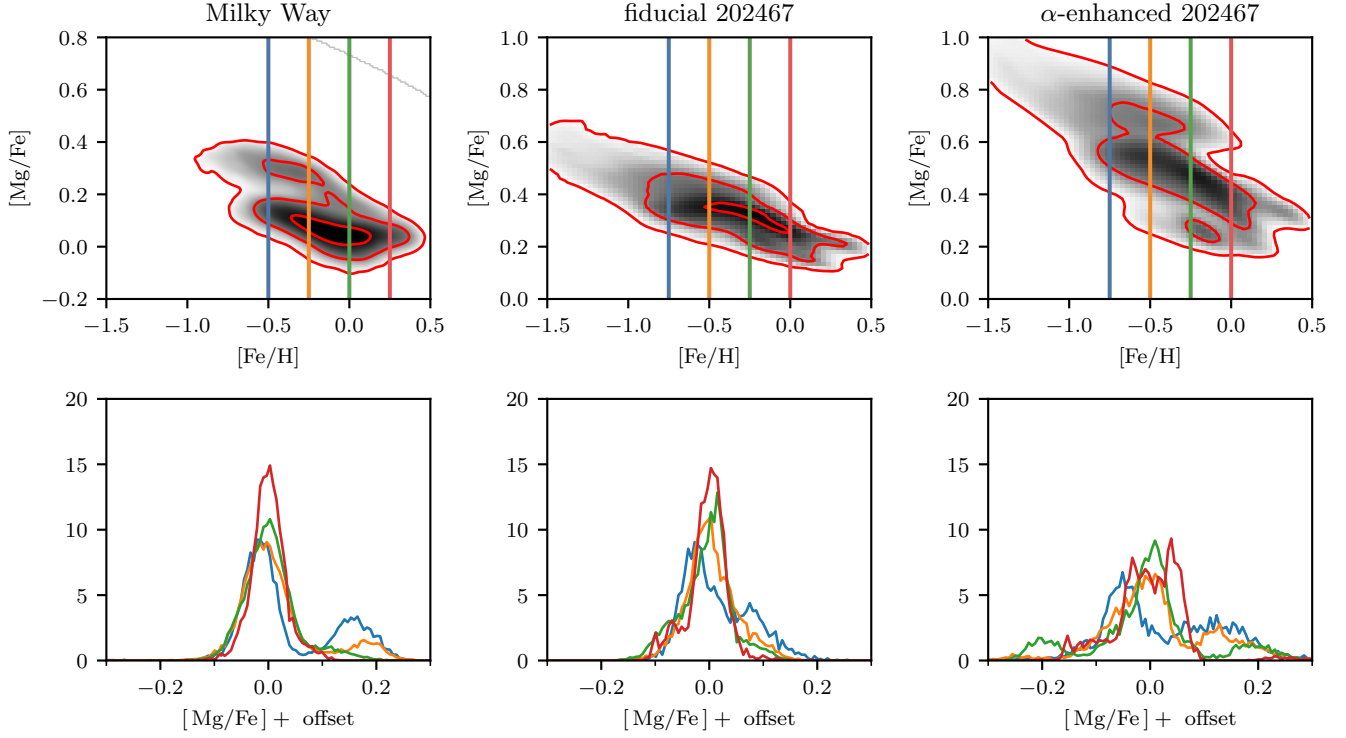


**Figure 13.** The same as Figure 1, but for a random subhalo from our catalog at  $z = 1.5$ .

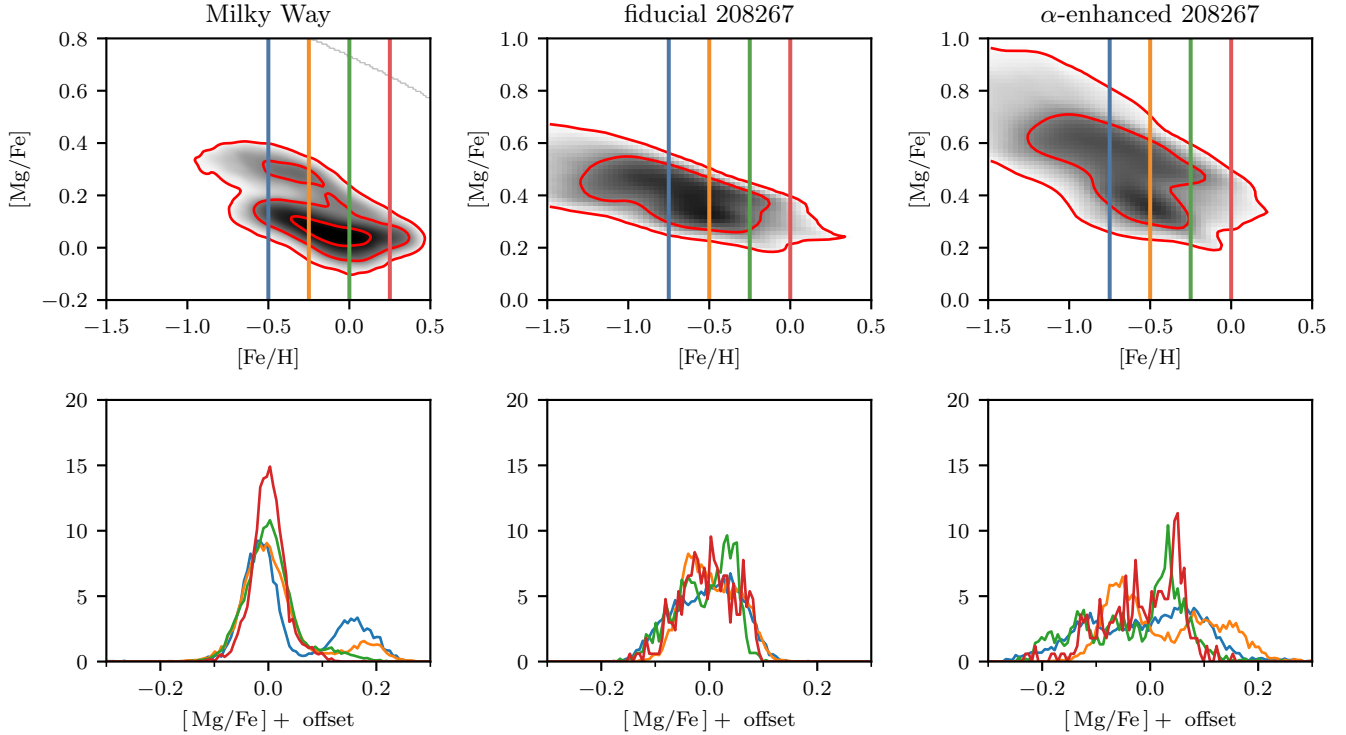


**Figure 14.** The same as Figure 1, but for a random subhalo from our catalog at  $z = 1.5$ .



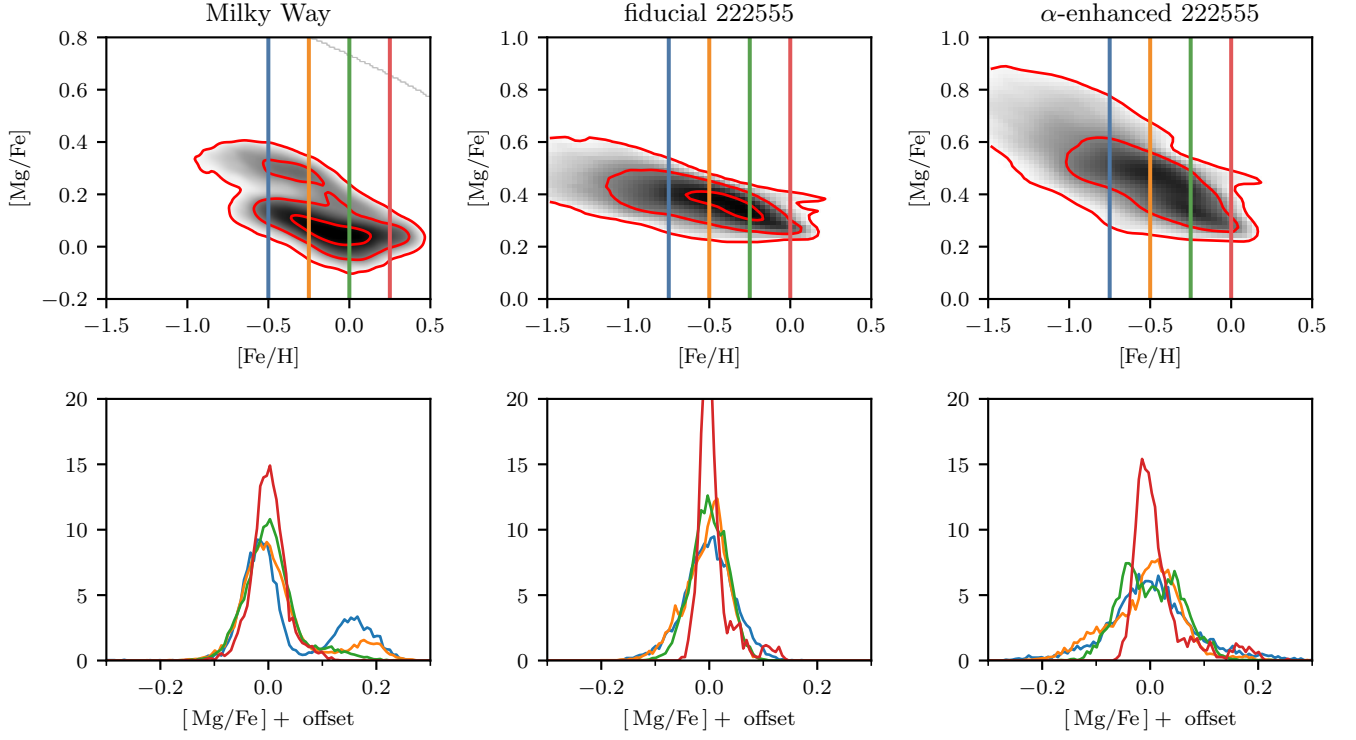


**Figure 15.** The same as Figure 1, but for a random subhalo from our catalog at  $z = 1.5$ .

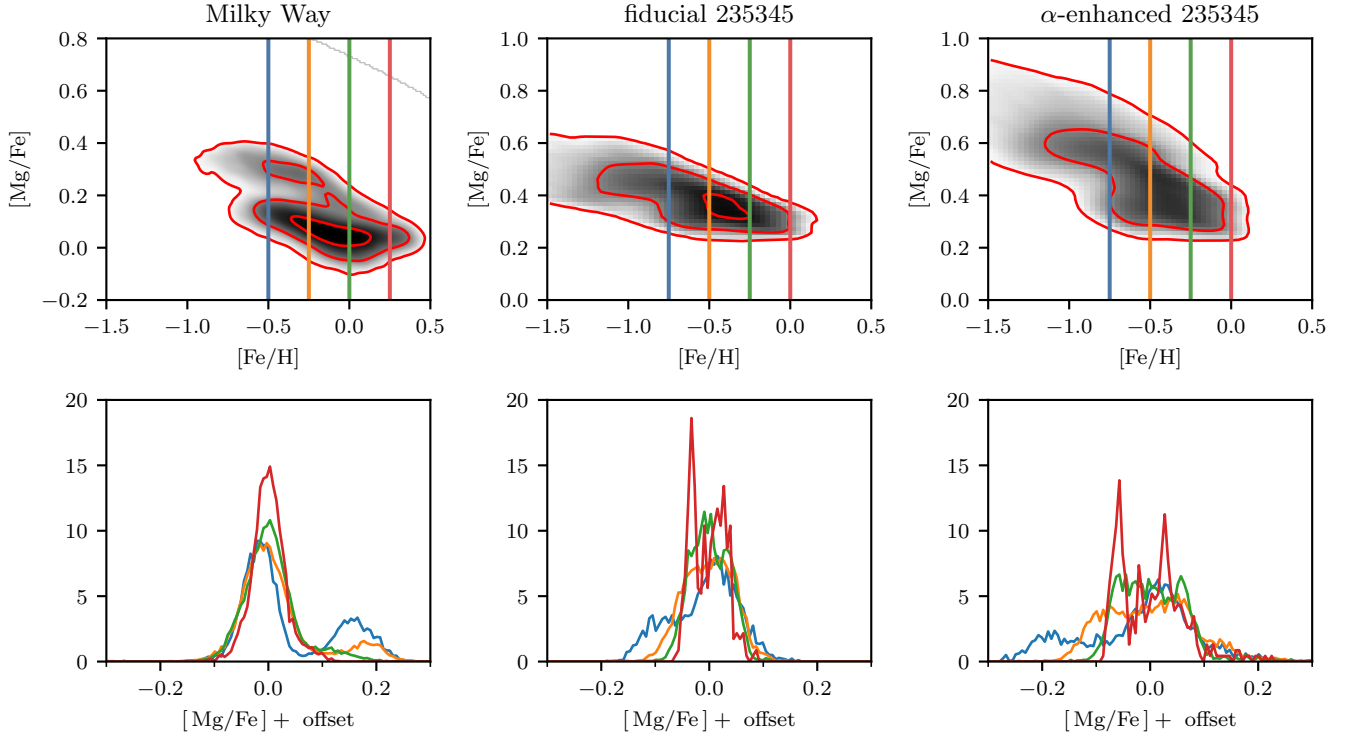


**Figure 16.** The same as Figure 1, but for a random subhalo from our catalog at  $z = 1.5$ .

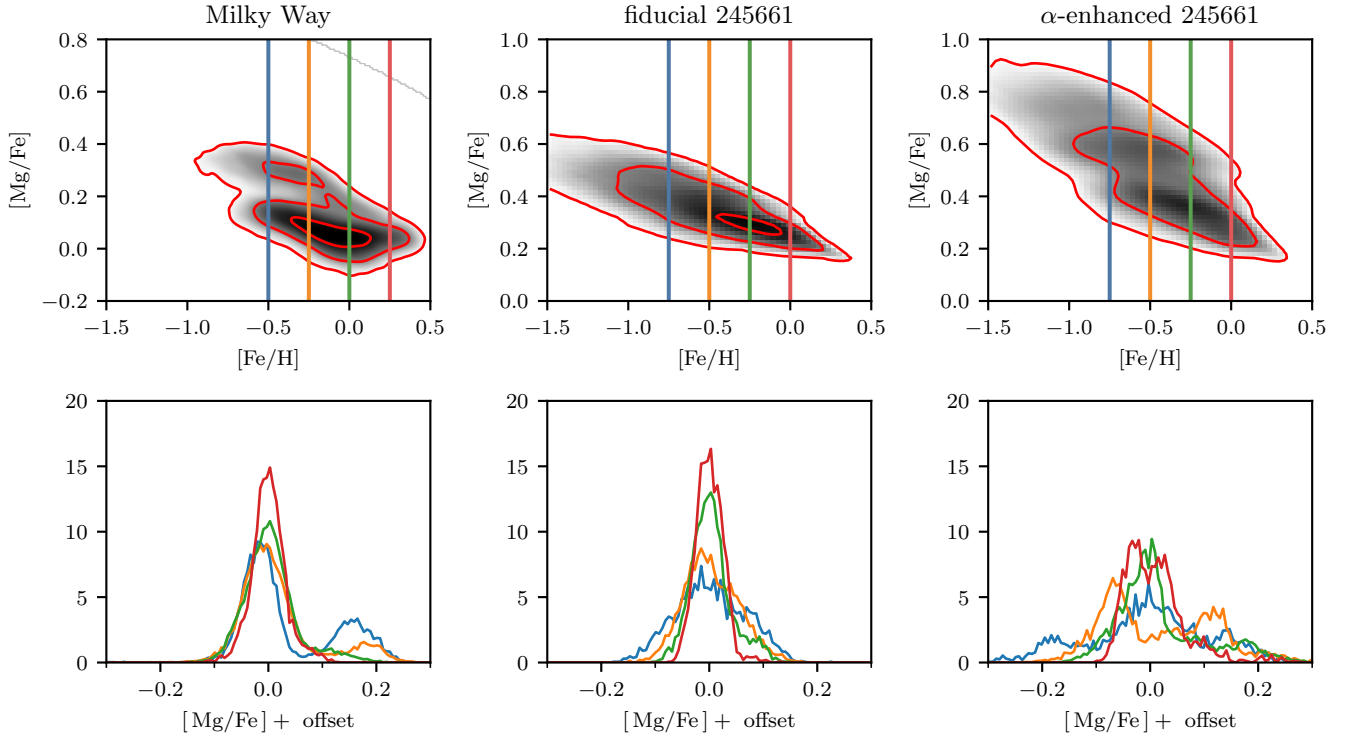


**Figure 17.** The same as Figure 1, but for a random subhalo from our catalog at  $z = 1.5$ .

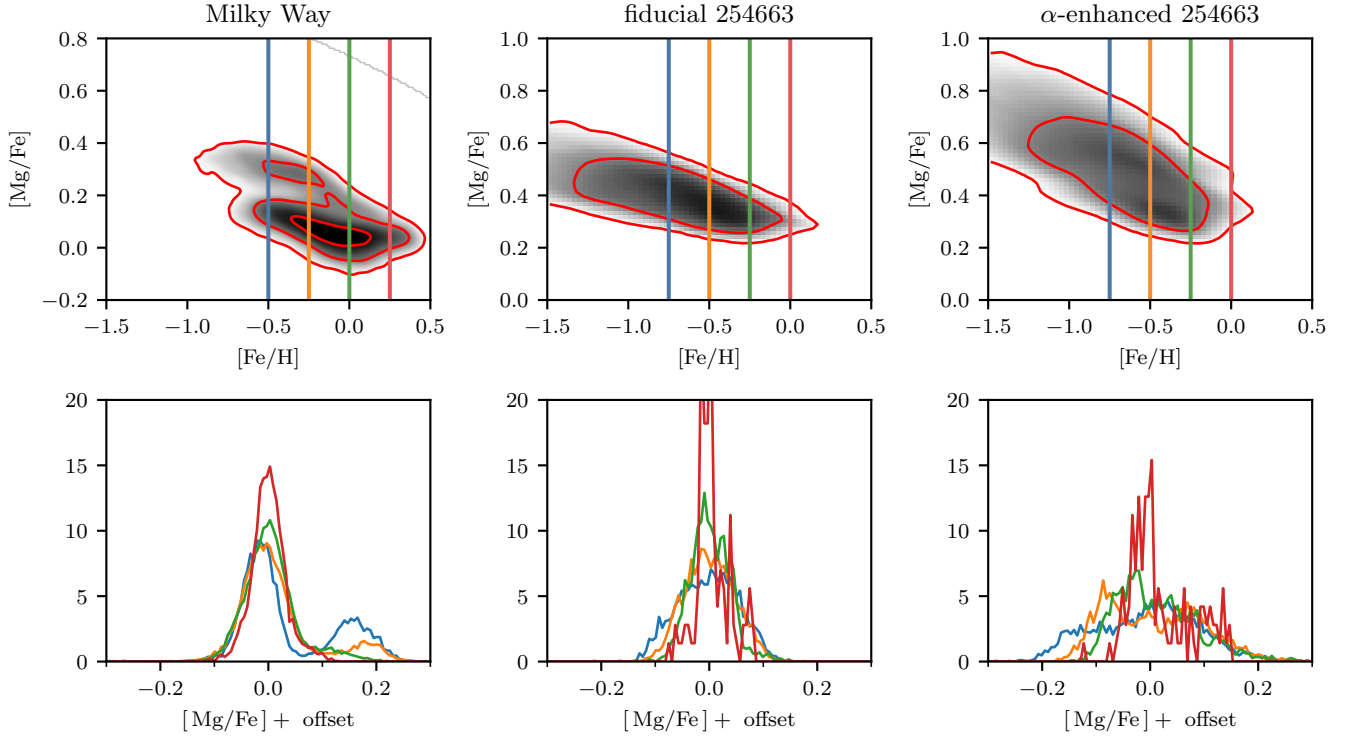


**Figure 18.** The same as Figure 1, but for a random subhalo from our catalog at  $z = 1.5$ .

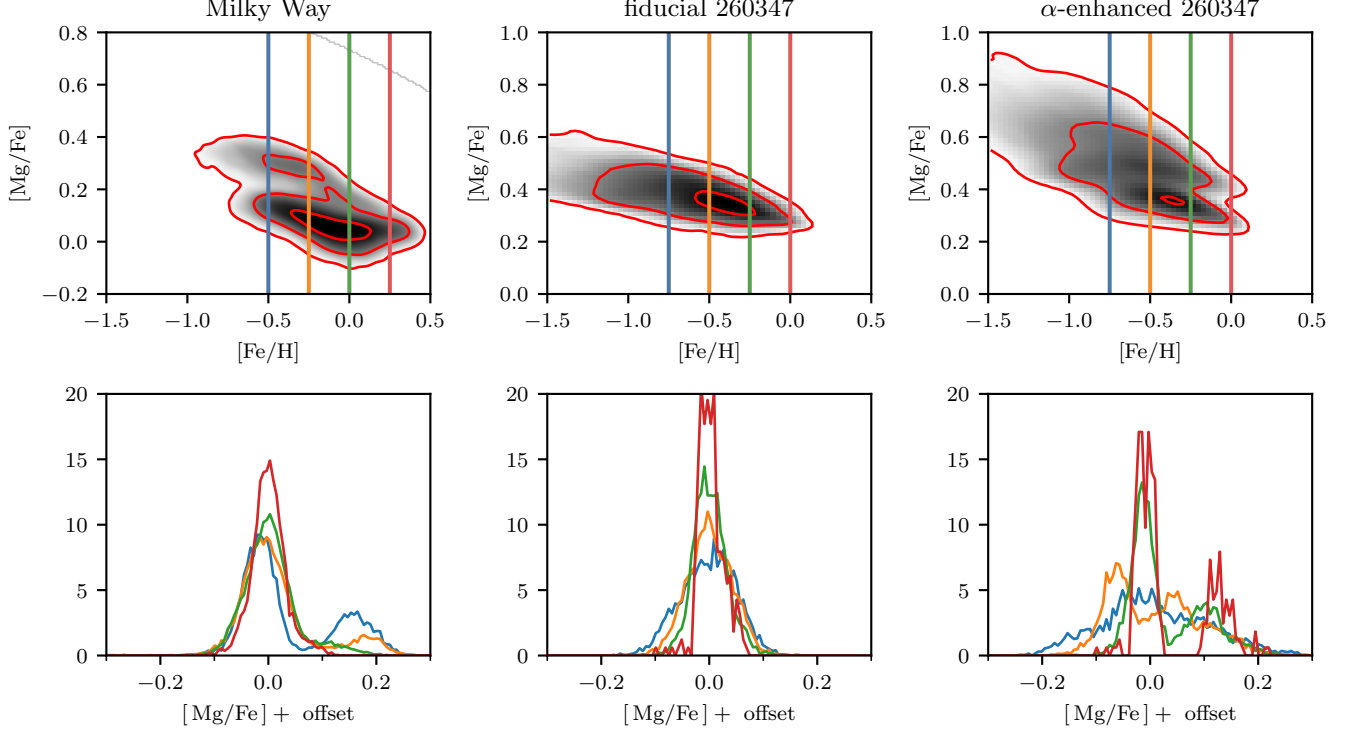


**Figure 19.** The same as Figure 1, but for a random subhalo from our catalog at  $z = 1.5$ .

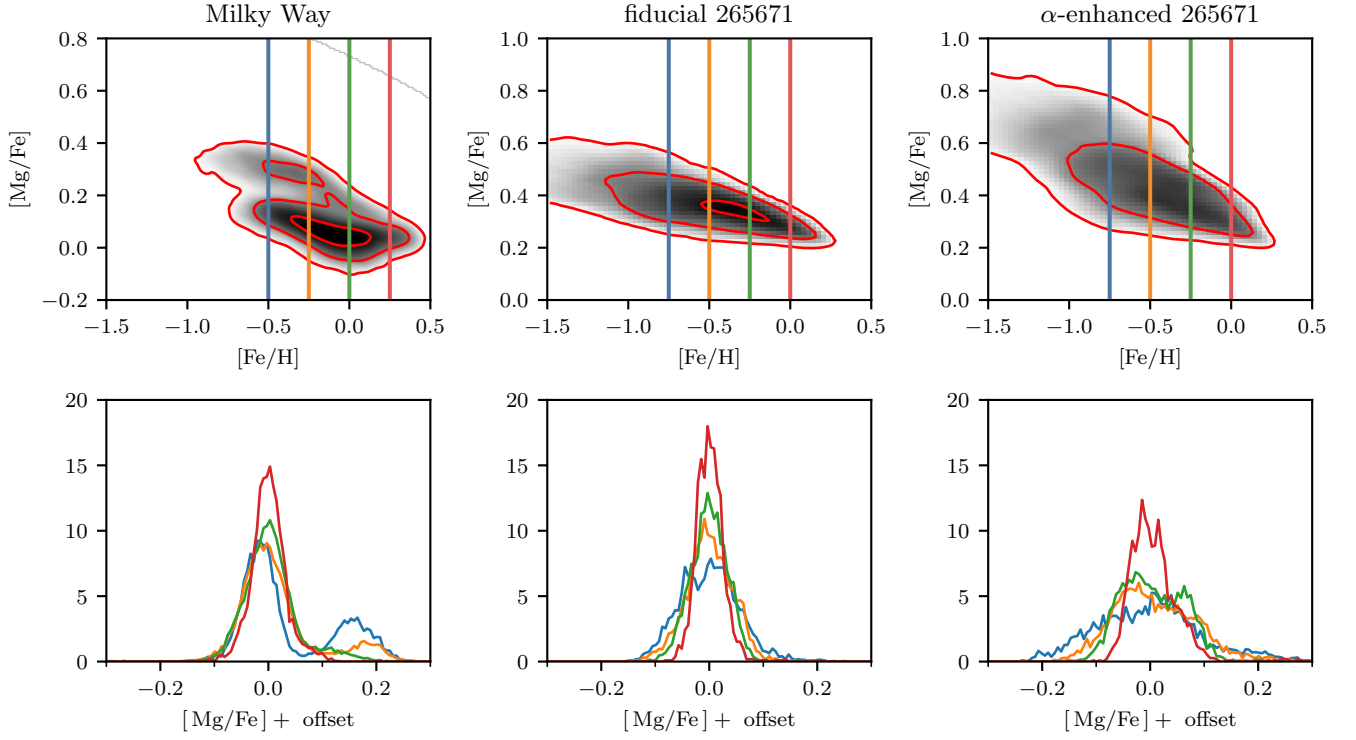


**Figure 20.** The same as Figure 1, but for a random subhalo from our catalog at  $z = 1.5$ .

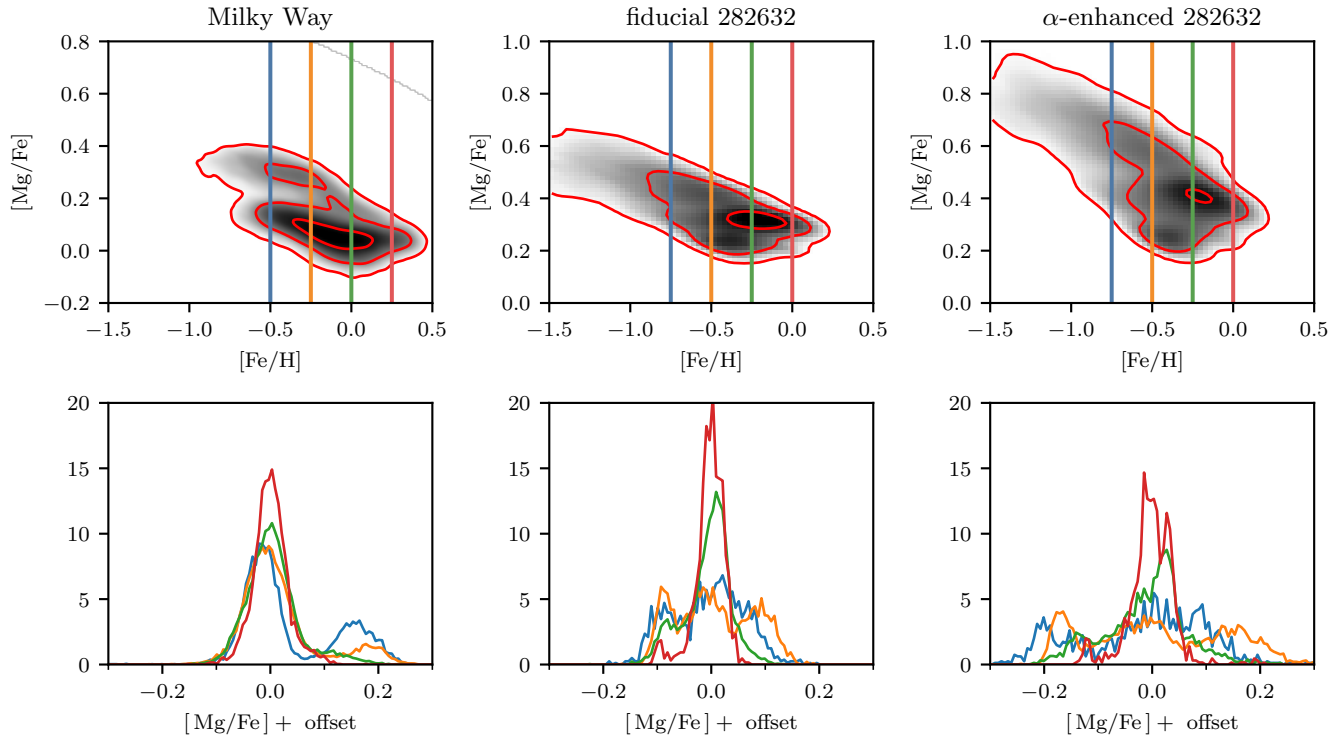


**Figure 21.** The same as Figure 1, but for a random subhalo from our catalog at  $z = 1.5$ .

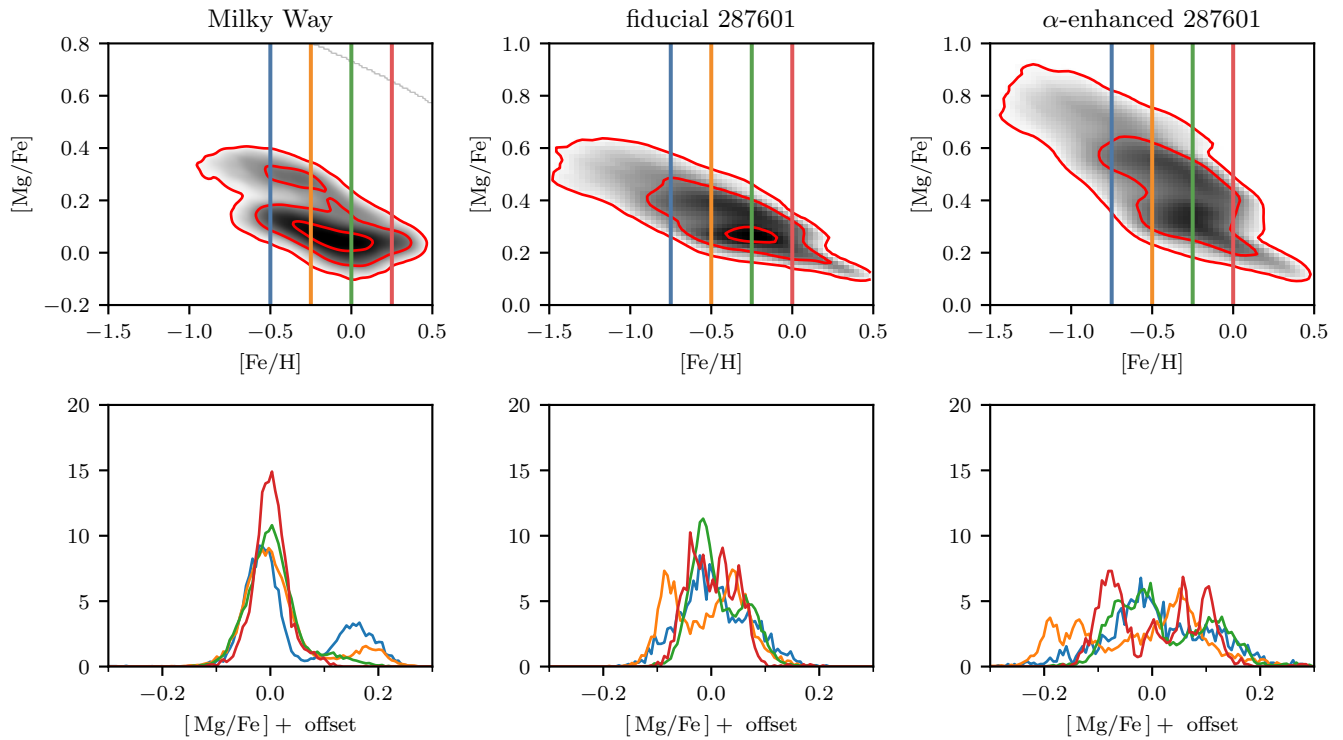


**Figure 22.** The same as Figure 1, but for a random subhalo from our catalog at  $z = 1.5$ .



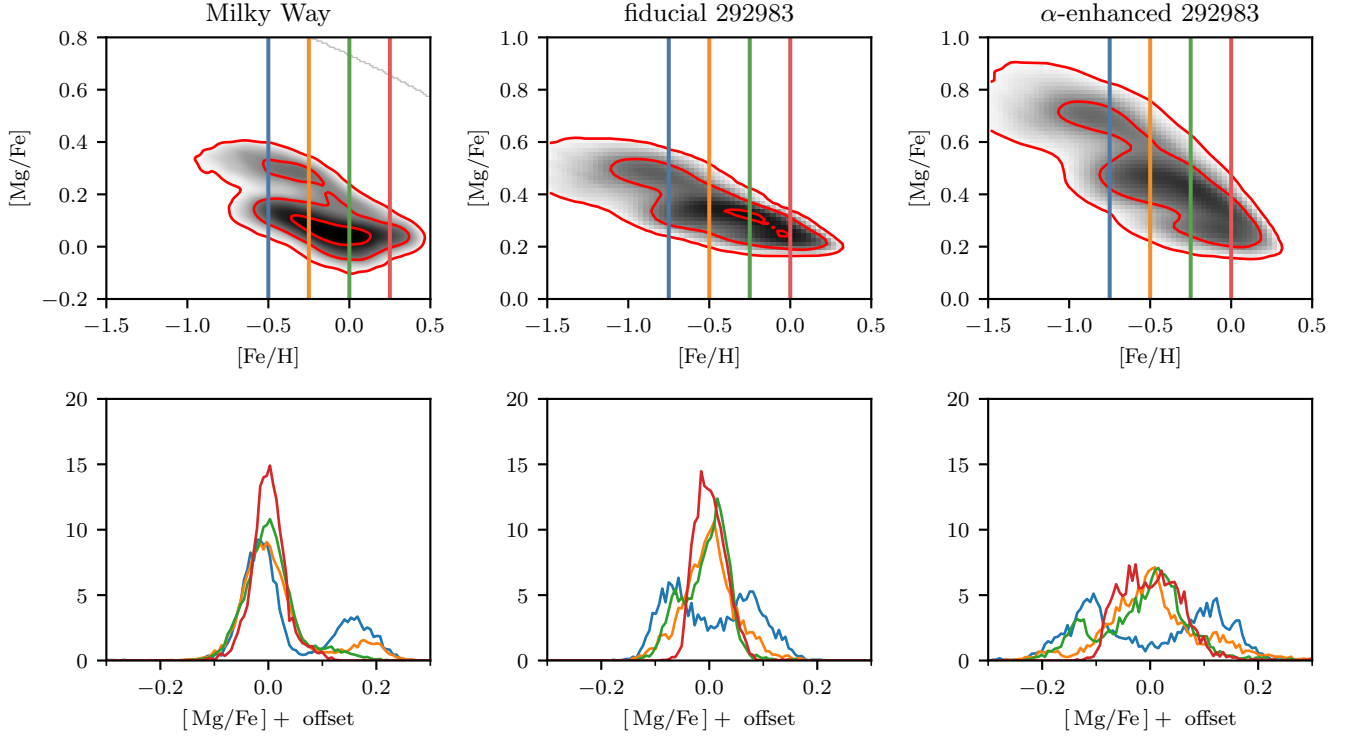


**Figure 23.** The same as Figure 1, but for a random subhalo from our catalog at  $z = 1.5$ .